Resonant scattering between dark matter and baryons: Revised direct detection and CMB limits

Xingchen Xu (许星辰)[*] and Glennys Farrar[†]

Center for Cosmology and Particle Physics, Department of Physics, New York University,
New York, New York 10003, USA

(Received 13 January 2022; accepted 28 April 2023; published 18 May 2023)

Traditional dark matter models, e.g., weakly interacting massive particles (WIMPs), assume dark matter (DM) is weakly coupled to the standard model so that elastic scattering between dark matter and baryons can be described perturbatively by the Born approximation; most direct detection experiments are analyzed according to that assumption. We show that when the fundamental DM-baryon interaction is attractive, dark matter-nucleus scattering is nonperturbative in much of the relevant parameter range. The cross section exhibits rich resonant behavior with a highly nontrivial dependence on atomic mass; furthermore, the extended rather than pointlike nature of nuclei significantly impacts the cross sections and must therefore be properly taken into account. The repulsive case also shows significant departures from perturbative predictions and also requires full numerical calculation. These nonperturbative effects change the boundaries of exclusion regions from existing direct detection, astrophysical and CMB constraints. Near a resonance value of the parameters the typical velocity-independent Yukawa behavior, $\sigma \sim v^0$, does not apply. We take the nontrivial velocity dependence into account in our analysis, however it turns out that this more accurate treatment has little impact on limits given current constraints. Correctly treating the extended size of the nucleus and doing an exact integration of the Schrödinger equation does have a major impact relative to past analyses based on the Born approximation and naive form factors, so those improvements are essential for interpreting observational constraints. We report the corrected exclusion regions superseding previous limits from XQC, CRESST Surface Run, CMB power spectrum and extensions with Lyman-α and Milky Way satellites, and Milky Way gas clouds. Some limits become weaker, by an order of magnitude or more, than previous bounds in the literature which were based on perturbation theory and pointlike sources, while others become stronger. Gaps which open by correct treatment of some particular constraint can sometimes be closed using a different constraint. We also discuss the dependence on mediator mass and give approximate expressions for the velocity dependence near a resonance. Sexaquark (*uuddss*) DM with mass around 2 GeV, which exchanges QCD mesons with baryons, remains unconstrained for most of the parameter space of interest. A statement in the literature that a DM-nucleus cross section larger than 10^{-25} cm^2 implies dark matter is composite, is corrected.

DOI: 10.1103/PhysRevD.107.095028

I. INTRODUCTION

A possible nongravitational interaction between dark matter and standard model particles is important both theoretically and experimentally. Such an interaction, if it exists, will have direct consequences for cosmology, astrophysics and direct detection experiments. For direct detection experiments and many astrophysical and cosmological applications the dark matter (DM) has nonrelativistic (NR) velocity $v \sim 10^{-3}c$, and this is the focus of this paper.

A nonrelativistic effective field theory was developed in Ref. [1] to generalize the commonly used spin-independent contact interaction to include nontrivial spin and momentum dependence in a systematic way, while staying within the framework of the Born approximation. If the Born approximation is applicable, the scaling with target nuclear mass *A* is simple [2] and the effects of a spatially extended source can be encoded by a form factor, as discussed in Sec. II C 1.

In this paper, we address the important but hitherto-not-properly-treated case when the interaction is strong enough that Born approximation does not apply. As we shall see, the correct treatment can dramatically change the interpretation of experiments—invalidating the Born approximation

---

[*] xingchen.xu@nyu.edu
[†] glennys.farrar@nyu.edu

scaling with A, invalidating the standard form factor treatment of nuclear size, and exhibiting, in general, strong resonance and antiresonance behavior of cross sections as a function of coupling and nuclear mass.

To expose these issues, we take the fundamental interaction to have a Yukawa form,

$$V(r) = -\frac{\alpha}{r} e^{-m_\phi r}, \tag{1}$$

sourced by an extended nucleon or nucleus.[1] When $m_\phi \to \infty$ this reduces to the widely used contact interaction, e.g., [2,3], having amplitude in the Born approximation

$$\mathcal{M} \sim g_\phi \bar{\chi}\chi \bar{N} N, \tag{2}$$

where g_ϕ is independent of momentum transfer q. The Yukawa potential is appropriate for any interaction described by a massive mediator and in the limit $m_\phi \to 0$ it becomes a Coulomb interaction.[2] Thus, while our choice of the form of the potential is not the most general conceivable, it is versatile and describes a large range of spin-independent interactions of interest.

In particular, the form of the potential we adopt is applicable to sexaquark dark matter (SDM) [4–6]. Our analysis is however general and the constraints we derive are applicable to beyond the Standard Model scenarios for a wide range of DM and mediator masses. In the SDM model, the dark matter is a scalar particle consisting of six standard model quarks ($uuddss$), with low enough mass that its lifetime is sufficiently greater than the age of the Universe. The upper limit on mass is $m_S \lesssim m_\Lambda + m_n \approx 2.05$ GeV, to ensure that its decay is doubly weak and the lifetime is longer than the age of the Universe, while a mass less than $\approx$1.7 GeV would be very difficult to reconcile with deuteron stability [6]. We adopt $m_S \sim 2m_p$ as a fiducial mass choice.

The interaction between sexaquark and baryon is mediated by the flavor singlet combination of ω and ϕ vector mesons. Thus the mediator mass m_ϕ is around the GeV scale for the sexaquark model, while for a hidden sector DM model m_ϕ could be quite different. The coupling strength α can naturally be as large as $\mathcal{O}(1)$, typical for a strong interaction process, although it could be much smaller depending on how ϕ couples to the DM. We will focus on the spin-independent (SI) cross section for simplicity here; for scalar DM including sexaquark DM, this is the only case.

Exact analytic solutions for the Yukawa potential scattering problem do not exist, and the Born approximation does not apply for the parameter space we are interested in. Moreover, the extended nature of the nucleon or nucleus sourcing the Yukawa potential means that the overall potential seen by the DM is not a Yukawa, even for a proton target. Therefore a full numerical solution of the Schrödinger equation is necessary. As we will see below, the typical cross section for the sexaquark model is around mb or 10^{-27} cm^2, if the DM and mediator masses are around a GeV and $\alpha \sim \mathcal{O}(1)$. Such a large cross section can be constrained by cosmological limits [7–9] and surface detectors [10–12], while deep underground detectors are mostly insensitive due to a thick overburden shading the DM flux [13].

Figure 1 shows the main current limits on the cross section as derived assuming the Born approximation. However, this parameter region is actually largely in the nonperturbative regime and the cross section has

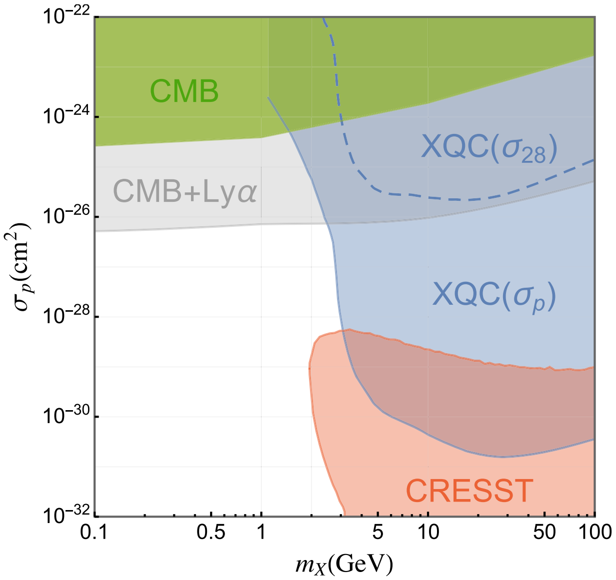

FIG. 1. Born-approximation-based DM-nucleon spin-independent cross section limits from XQC [12] (blue); CMB (green) and CMB + Lyman-α (gray) [9]; and CRESST surface detector (red) [12,16]. The dashed line is the limit on the DM-Si cross section, σ_{28}, which is the actual constraint from XQC. For XQC and CRESST we display the limit corresponding to a thermalization efficiency of 0.01; simple estimates suggest a higher efficiency is questionable so to obtain a robust and conservative upper bound a higher efficiency should not be adopted [6,12]. A measurement of the thermalization efficiency is critically needed. To reiterate, the limits shown in this plot are generally invalid and must be replaced by those in Fig. 14 obtained using a fully nonperturbative treatment.

---

[1] The minus sign in Eq. (1) is for convenience so that $\alpha > 0$ corresponds to an attractive potential; in Sec. V B and associated figures dealing with the repulsive case, we use Eq. (1) without the minus sign to keep α positive. In this paper we devote greatest attention to the attractive case because of its rich and sometimes dramatic phenomenology; the repulsive case is treated as well.

[2] Were constraints on dark photon and millicharged DM models not already so strong, our analysis would be relevant for those models as well. As is, due to the weak coupling strength, the Born approximation is adequate and our more general treatment is not needed.

a nontrivial dependence on all of the parameters $(m_X, m_A, r_A, m_\phi, \alpha)$, where A is the atomic mass number and $\{m_A, r_A\}$ are the target nucleus mass and radius. Without the Born approximation, there is no *a priori* relationship between the cross section on nucleus A and that on a proton. This makes it nontrivial to translate from the actual experiment measuring the interaction between DM and detector material, to the coupling strength parameter α or the DM-nucleon cross section $(A = 1)$.[3] Here we provide this linkage, for the key constraining experiments and observations.

In our analysis for the attractive interaction, resonant scattering plays an important role. The resonance we are talking about in this context should not be confused with the Breit-Wigner resonance typically seen in high-energy physics. A Breit-Wigner resonance generally appears as a peak at certain center of mass energy in the function $\sigma(v)$ or $\sigma(E)$ and is usually associated with excitation of some intermediate state, see Ref. [17] for example. Rather, the resonance we encounter here is the low-energy elastic scattering s-wave resonance, which corresponds to a zero-energy bound state of the scattering potential. As a result the resonance appears as a peak of the cross section at some particular parameter values (α, m_ϕ, m_X, A) which do not depend on velocity. For low-energy scattering, $\sigma \sim v^{-2}$ on the resonance while $\sigma \sim v^0$ off the resonance. The fact that dark matter has a velocity distribution does not smooth out the resonance as a function of the model parameters, contrary to what is perceived in [15]. For certain parameter choices it is possible to have a p-wave or higher wave Breit-Wigner resonance in $\sigma(v)$, which is associated with a quasibound state of the effective potential including the angular term. Such higher partial-wave resonances are less relevant for us as they require higher energy and are usually subdominant to the s-wave contribution. The transition to the classical regime entails an arbitrarily large number of partial waves. If one wants to make an analogy, the nonperturbative cross section and s-wave resonance here are closely related to the Sommerfield enhancement of DM annihilation and freeze out [18–20]. In fact, resumming all box diagrams responsible for the Sommerfield enhancement has been shown to approximately recover the numerical solution of the Schrödinger equation in the appropriate regime.

Although motivated in large part by the sexaquark, our results are more general and applicable to any interaction described by a Yukawa potential as results from CP-even scalar or vector mediator in the nonrelativistic quantum regime, sourced by an extended nuclear distribution. The experimental constraints obtained here can be directly applied to any DM model with mediator mass above a few hundred MeV, using a scaling law we derive. For lower mediator mass the methodology is applicable but the numerical experimental limits need to be recalculated as we do for several illustrative cases. Our results can be applied to interactions within a complex hidden sector as well. We take the dark matter particle to be pointlike, but our techniques are applicable to extended dark matter case and general features of our results apply there as well.

This paper is organized as follows. In Sec. II we show some general results on nonperturbative effects and their application to experimental results, especially the resonant behavior, the nontrivial atomic mass (A) scaling of the cross section, and the special behavior of nuclear form factor in resonant regime. In Secs. III and IV we present how to reinterpret the result of direct detection experiments and astrophysical and cosmological constraints in this nonperturbative regime. We give the combined constraints on parameter space in Sec. V A for attractive interaction and Sec. V B for repulsive, discuss dependence on mediator mass in Sec. V C and conclude in Sec. VI. Our numerical methods for calculating the DM-baryon scattering cross sections are described in the Appendix A, where an approximate expression for the velocity dependence near a resonance is also derived.

II. YUKAWA INTERACTION WITH EXTENDED SOURCE

A. Source model

In a realistic model where a nucleus is the source for the potential scattering of a DM particle, the source has a specified matter distribution rather than being a singular point as in the simple Yukawa of Eq. (1). The Yukawa charge is then smeared out with some charge density and the potential becomes

$$V(\vec{r}) = \int -\frac{\alpha\rho(\vec{r}')}{|\vec{r} - \vec{r}'|} e^{-m_\phi|\vec{r}-\vec{r}'|} d^3\vec{r}', \tag{3}$$

where $\rho(\vec{r}')$ is the normalized Yukawa-charge distribution of the source with normalization

$$\int \rho(\vec{r}') d^3 r' = 1. \tag{4}$$

For example a point source has $\rho(\vec{r}') = \delta(\vec{r}')$. The finite size of the source regulates the Yukawa potential at the origin and thus influences the cross section.

We adopt in this paper a simple model for the nuclear density distribution as being a uniform ball with radius r_0, which we identify as the radius of the nucleus,

---

[3] We presented our results on the generic failure of the Born approximation scaling relation for DM scattering on nuclei through a Yukawa potential in [14]. Subsequently, Ref. [15] considered a repulsive square-well potential and contact interaction for massive dark matter, showing that the Born approximation applies for DM-proton scattering only if $\sigma_p \ll 10^{-25}$ cm^2, and that for xenon (A = 131) Born scaling fails when $\sigma_p \gtrsim 10^{-32}$ cm^2. See Sec. V D regarding an inaccurate assertion in that paper [15].

$$\rho(\vec{r}') = \begin{cases} \frac{3}{4\pi r_0^3} & (r' < r_0) \\ 0 & (r' \geq r_0) \end{cases}. \tag{5}$$

The corresponding rms radius is 0.77 r_0, so given that the proton charge radius is 0.8 fm, we take $r_0 = 1$ fm for the proton. We take $r_0 = R_0 A^{\frac{1}{3}} \equiv \mathrm{fm}$ for nucleus of mass number A with $R_0 = 1.0$ fm. This is a common description of the nucleus and was adopted previously for the binding of sexaquark with nuclei [21]. It suffices for displaying the features of the extended distribution, which is our aim in this paper. We check the sensitivity of results to R_0 by also calculating for $R_0 = 1.2$ fm and find that the detailed position of resonance and antiresonance features are sensitive to R_0 and the profile of the density distribution, so limits would vary somewhat if a smoother nuclear wave function or different R_0 were adopted.

Integrating Eq. (3) to get the potential, we find

$$V(r) = -\frac{3\alpha}{m_\phi^2 r_0^3} \times \begin{cases} 1-(1+m_\phi r_0)e^{-m_\phi r_0}\frac{\sinh(m_\phi r)}{m_\phi r} & (r<r_0) \\ [m_\phi r_0 \cosh(m_\phi r_0) - \sinh(m_\phi r_0)]\frac{e^{-m_\phi r}}{m_\phi r} & (r \geq r_0). \end{cases} \tag{6}$$

Now, a new length scale r_0 has been introduced in addition to the Yukawa screening length $\lambda = 1/m_\phi$. In the limit $r_0 \ll \lambda$ we recover the point Yukawa potential (1). When $r_0 \gg \lambda$, inside the ball, the potential is essentially constant,

$$V(r) \xrightarrow{r_0 \gg \lambda} -\frac{3\alpha}{m_\phi^2 r_0^3} \quad (r < r_0). \tag{7}$$

So the potential is a square well with radius r_0, with a soft transition region at the boundary whose width is λ. The range of the potential is now primarily determined by r_0 instead of λ, when $r_0 \gg \lambda$—as is the case for $\lambda^{-1} \approx$ GeV as relevant for flavor singlet hadronic interactions, especially for heavy nuclei.

B. General results in the nonperturbative regime

As discussed in the Appendix A, it is useful to write everything in dimensionless language. For the simple Yukawa of Eq. (1) and in the nonrelativistic limit, two parameters suffice [22],

$$a \equiv \frac{v}{2\alpha}, \qquad b \equiv \frac{2\mu\alpha}{m_\phi}, \tag{8}$$

with μ the reduced mass and v the relative velocity. To describe the extended nucleus we introduce a third dimensionless parameter c, with

$$\frac{c}{b} \equiv \frac{r_0}{\lambda} = m_\phi r_0, \tag{9}$$

so the dimensionless potential $\tilde{V}(x)$ in the Schrödinger equation (A7) becomes, with $x \equiv 2\mu\alpha r$,

$$\tilde{V}(x) = -3\left(\frac{b}{c}\right)^3 \times \begin{cases} \frac{1}{b} - (1+\frac{c}{b})e^{-\frac{c}{b}}\frac{1}{x}\sinh(\frac{x}{b}) & (x<c) \\ [\frac{c}{b}\cosh(\frac{c}{b}) - \sinh(\frac{c}{b})]\frac{1}{x}e^{-\frac{x}{b}} & (x \geq c) \end{cases}. \tag{10}$$

We then use the methods described in the Appendix A to solve for the cross section.

Figures 2 and 3 show σm_ϕ^2 as a function of the dimensionless parameters (a, b) for the point source potential. It is obvious that the cross section is not a smooth function of the underlying parameters. For the extended potential the behaviors are similar, with shifted locations of the resonances and antiresonances. Figure 16

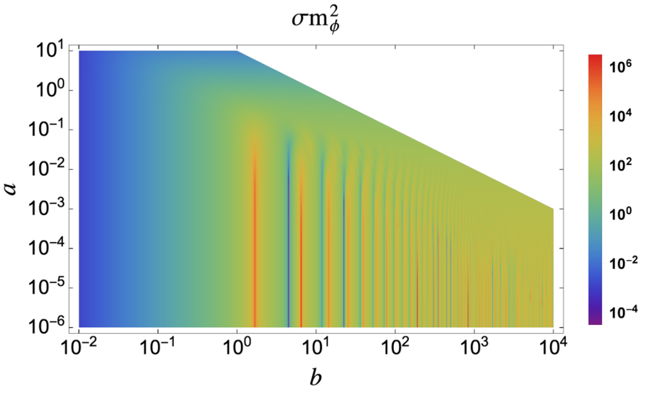

FIG. 2. 2D plot of σm_ϕ^2 as a function of (a, b) for a point source, with σm_ϕ^2 shown by colors. The cutoff in the upper-right corner is where $ab \geq 10$, which is the classical regime.

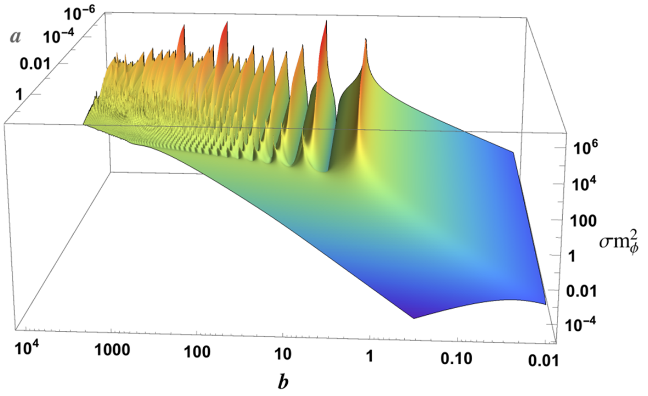

FIG. 3. 3D plot of σm_ϕ^2 as a function of (a, b) for a point source, with σm_ϕ^2 along the z-axis. The "crenellated" appearance is merely a sampling artifact due to the resolution of the figure.

in the Appendix B shows the profile for several values of c/b in comparison to a square well.

1. Distinct regimes of parameter space

(a) *Classical regime* ($ab \gg 1$)*:* The upper right corner in Fig. 2 (which is the lower-left corner in Fig. 3) is cut out beyond $ab = \mu v/m_\phi \geq 10$. In this regime the de Broglie wavelength of the particle is much smaller than the typical scale of the potential and classical mechanics is sufficient to describe the scattering. In this regime there are already some nonperturbative effects relevant in plasma physics where a screened Coulomb potential is used [23]. Reference [24] considered this regime in trying to solve astrophysical problems with self-interacting dark matter (SIDM) models. Outside this region, when $ab \lesssim 1$, a classical treatment fails and quantum effects need to be included.

(b) *Born regime* ($b \ll 1$)*:* The blue region with relatively small cross section and $b \ll 1$ is the Born regime where perturbative calculation is reliable.

(c) *Quantum resonant regime* ($ab \lesssim 1$ *and* $b \gtrsim 1$)*:* The region between the classical and the Born regime is the quantum-resonant regime where the scattering problem is entirely quantum mechanical and nonperturbative. The resonant behavior of the cross section is clear in Figs. 2 and 3. We are mostly interested in this regime where analytic description is absent and numerical calculation is a must. One model which falls in this regime is sexaquark dark matter, which has $m_X \sim 2$ GeV and a mediator $m_\phi \sim 1$ GeV with coupling possibly as large as $\alpha \sim 1$ to nucleon. For a sexaquark colliding with silicon ($m_A \approx 28 m_p \approx 26.3$ GeV) at $v = 300$ km/s, the corresponding parameters are $a = 0.0005$, $b = 3.71$, and $ab = 0.0019$.

For the extended potential we can almost draw the same conclusions, except that when $c \gg b$, the range of the potential is determined by r_0 rather than $1/m_\phi$, and the quantum resonant regime is determined by $ac \ll 1$. Taking the same sexaquark-silicon collision as an example and using $\sim A^{\frac{1}{3}}$ fm to approximate the silicon nucleus radius, we find $c/b \sim 15$ and $ac \sim 0.03$, which falls well in the quantum-resonant regime.

2. Resonance and antiresonance

The strong enhancement or diminution of cross section in the resonant regime can be understood from the phase shift. In the parameter regime that the Born approximation is valid, the cross section is

$$\sigma^{\mathrm{Born}} = \frac{4\pi b^2}{m_\phi^2 (1 + 4a^2 b^2)}, \tag{11}$$

but this cannot be applied to the resonant regime. The general result at low energy when s-wave ($l = 0$) scattering is dominant (which is usually true for us, as we will see later) is, from Eq. (A11),

$$\sigma_{\text{s-wave}} = \frac{4\pi}{a^2 b^2 m_\phi^2} \sin^2(\delta_0), \tag{12}$$

where δ_0 depends on a, b, c; δ_0 must be calculated numerically in the resonant regime. When $\delta_0 \to \frac{\pi}{2}$ the cross section is on resonance and reaches its maximum value, resulting in the peaks in Figs. 2 and 3. The position of the peaks is in one-to-one correspondence with the zero-energy bound states of the Yukawa potential. In the pointlike source problem ($c = 0$), the potential is $e^{-\frac{x}{b}}$, with b setting its range. When $b \ll 1$ the potential is too narrow and weak to accommodate any bound states. As b increases, the potential becomes wider and stronger up to the point where a bound state with $E_0 \to 0^-$ emerges, in which case the scattering cross section reaches its maximum. As b continues to increase, the ground state binding energy gets more and more negative, up to some point where another bound state with $E_1 \to 0^-$ emerges and the scattering cross section hits another peak. The position of these zero-energy bound states are easily calculated to be at $b = 1.68$, 6.45, 14.34, etc., which are exactly the locations of the peaks in Figs. 2 and 3. On the other hand when $\delta_0 \to n\pi$ the cross section $\sigma_{\text{s-wave}} \to 0$, which is an antiresonance and corresponds to the valleys in Figs. 2 and 3. The reduced cross section at antiresonances in the parameter space is responsible for evading some experimental limits on the DM-baryon scattering cross section. The antiresonances are not associated with any bound state. For an extended potential we have similar resonances and antiresonances, they just appear at different b values. In general, the location of the (anti)resonance is a function of c/b.

3. S-wave dominance

It is usually the case that at low energy, s-wave scattering is dominant. In terms of (a, b) this means small a. Figure 4 shows $l_{\max}$, such that the contribution to the total cross section of partial waves from $l = 0$ to $l = l_{\max}$ is more than

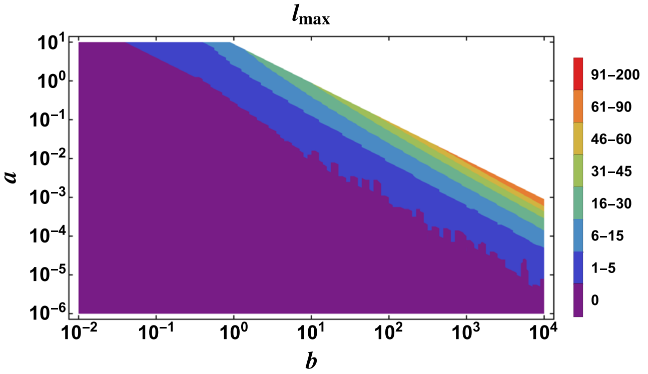

FIG. 4. $l_{\max}$ in the (a, b) plane.

99%. We see that for a pure Yukawa interaction with $ab \ll 1$, the scattering is always s-wave dominated and quantum mechanical. For an extended potential, s-wave dominance also requires $ac \ll 1$. This is however also the condition for quantum resonant scattering, so the cross section for the extended potential in the resonant regime is automatically s-wave dominated and hence isotropic in the center-of-mass frame. This simplifies the expressions for the event rate of DM direct detection experiments.

4. Born approximation validity

The Born approximation applies when $b \ll 1$. To quantify this, Fig. 5 shows the ratio of cross sections calculated by the Born approximation and by numerical solution. The Born approximation is within ±10% of the exact result for $b \lesssim 0.1$. This is also generally true for the extended potential.

5. Velocity dependence

Another feature in the quantum resonant regime is that the cross section may have nontrivial velocity dependence, whereas the Born approximation generally has no velocity dependence at small velocity. Figure 6 shows $\sigma m_\phi(v)$ for some illustrative values of b. At small velocity we have several different behaviors:

(i) On resonance ($b = 1.68$), $\sigma \sim v^{-2}$, i.e., greatly enhanced at small v. Here, s-wave unitarity fixes the cross section at the peak of the resonance. Using (12), with $\sin^2(\delta_0) = 1$ gives

$$\sigma_{\rm res} = \frac{4\pi}{\mu^2 v^2} = 4.9\times 10^{-21}\ {\rm cm}^2 \left(\frac{\rm GeV}{\mu}\frac{10^{-3}c}{v}\right)^2 \tag{13}$$

with negligible contribution from other partial waves. Note the cross section becomes independent of A, coupling, and source size.

(ii) At antiresonance ($b = 4.52$), the s-wave contribution to σ vanishes and only the very small higher partial waves contribute. The antiresonances are in general away from any resonance for a different A or l and are therefore independent of velocity.

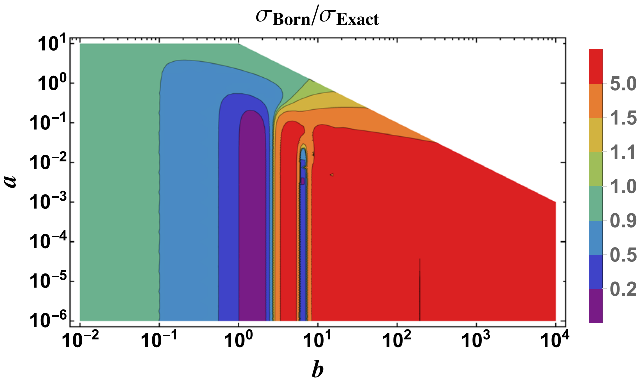

FIG. 5. Ratio of $\sigma_{\rm Born}$ over $\sigma_{\rm Exact}$.

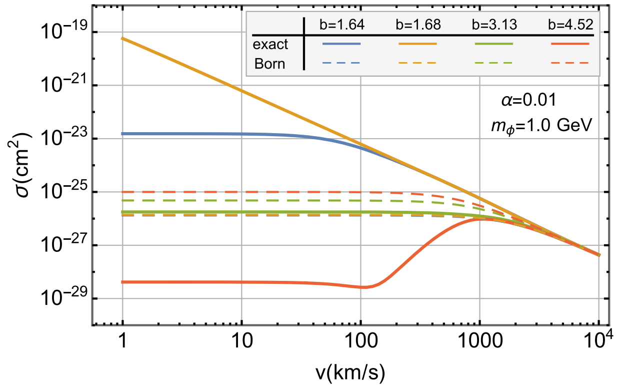

FIG. 6. Velocity dependence of the cross section for four values of $b \equiv 2\mu\alpha/m_\phi$; $b = 1.68$ (tan) is on resonance and $b = 4.52$ (red) is on antiresonance.

(iii) For b values well-separated from resonance and antiresonance, $\sigma \sim v^0$ (independent of velocity) up to a large velocity whose value depends on parameters. At such large velocities there is no simple expression for a general source distribution, but for a point Yukawa the scattering becomes Coulomb-like, so at sufficiently high v, $\sigma \sim v^{-4}$ for all b.

Near but not on a resonance, there is a transition in behavior around $v \sim v^*$ with $\sigma \sim v^{-2}$ for $v \gg v^*$ and $\sigma \sim$ constant for $v \ll v^*$. In Appendix B a useful approximate expression for the velocity dependence near resonant values of α is derived, valid when the radius r_0 of the extended Yukawa is large enough that it can be approximated as a square well. Near the first resonance,

$$\sigma \to 4\pi/(\mu v)^2 \qquad v \gg v^* \tag{14}$$

and

$$\sigma \to \frac{8 m_\phi^2 r_0^3}{3\pi\mu(\sqrt{\alpha} - \sqrt{\alpha_{\rm res}})^2} \qquad v \ll v^* \tag{15}$$

with

$$v^* \equiv \frac{\pi|\sqrt{\alpha} - \sqrt{\alpha_{\rm res}}|}{m_\phi r_0 \sqrt{2\mu r_0/3}}, \tag{16}$$

and

$$\alpha_{\rm res} \equiv \left(\frac{\pi}{2}\right)^2 \frac{m_\phi^2 r_0}{6\mu}. \tag{17}$$

A standard way to characterize the cross section and its velocity dependence at low energy ($k \to 0$) is by introducing the scattering length in an effective range expansion (see, e.g., Ref. [25] Chapter 6.6). In the low-energy limit the total cross section is dominated by s-wave scattering and can be expressed in terms of the s-wave phase shift δ_0 and momentum $k = \mu v$ for small k,

$$\sigma \approx \sigma_{l=0} = \frac{4\pi}{k^2} \sin^2 \delta_0 = \frac{4\pi}{k^2 + k^2 \cot^2 \delta_0}. \tag{18}$$

In the effective range expansion, $k \cot \delta_0$ is expanded as a series in k,

$$k \cot \delta_0 \equiv -\frac{1}{a} + \frac{1}{2} r_{\text{eff}} k^2 + \mathcal{O}(k^4). \tag{19}$$

The coefficients of the first two terms are given special names: a is called the "scattering length" and r_{eff} the "effective range."[4] Near a resonance, the effective range expansion (19) is a good approximation with $|a| \gg r_{\text{eff}}$ and the cross section can be expressed as

$$\sigma \approx \frac{4\pi}{\frac{1}{a^2} + (1 - \frac{r_{\text{eff}}}{a}) k^2}. \tag{20}$$

In the denominator of Eq. (20) we have neglected terms of order $\mathcal{O}(k^4)$, including the term $1/4 r_{\text{eff}}^2 k^4$. While much smaller than the ones we kept, this term is required to keep the cross section smaller than the unitarity limit, $4\pi/k^2$, as pointed out by Schwinger [26].

Exactly on resonance, the scattering length is infinite and we have $\sigma \approx 4\pi/k^2$ down to arbitrarily low velocities, as in Eq. (13). When the scattering is near but not on resonance, a is finite and Eq. (20) tells us the velocity dependence is $\sigma \sim$ constant for small k and $\sigma \sim v^{-2}$ for large k,

$$\sigma \approx \begin{cases} 4\pi a^2 = \frac{4\pi}{k^2} & (k|a| \ll 1 \text{ or } v \ll v^*) \\ \frac{4\pi}{k^2} & (k|a| \gg 1 \text{ or } v \gg v^*). \end{cases} \tag{21}$$

The transition happens at $k^*|a| \approx 1$ or

$$v^* \approx \frac{2}{\mu} \sqrt{\frac{\pi}{\sigma_0}}, \tag{22}$$

where $\sigma_0 \equiv \lim_{v \to 0} \sigma$ and $k^* \equiv \mu v^*$. The cross section at low velocity $v < v^*$ approximately saturates at the unitarity bound at the transition velocity $v = v^*$. Far from the resonance, the $r_{\text{eff}} k^2$ and higher-order terms are important, so Eq. (20) is not accurate and the velocity dependence must be determined including those higher-order terms. Examples of these behaviors are shown in Fig. 6 for different parameters; the antiresonance case is an example where the effective range expansion (19) is insufficient [27,28].

Figure 6 and Eqs. (20) and (21) provide guidance for when the cross section's velocity dependence needs to be taken into account in an analysis. Figure 6 shows that except near an antiresonance, the cross section is generically velocity independent at low velocity, but falls as v^{-2} above some velocity we designate as v^*. As long as the velocity of most of the DM with respect to the detector is below v^*, the cross section can be taken as constant, σ_0; otherwise, the velocity dependence needs to be incorporated into the analysis. But the magnitude of σ_0 is related to the break velocity v^*, through Eq. (22). Thus, if a cross section value under investigation satisfies

$$\sigma \lesssim \sigma_{\text{max}} \equiv \frac{4\pi}{(\mu v_{\text{max}})^2}, \tag{23}$$

where v_{max} is the maximum relative velocity of the DM and detector and μ is the reduced mass, then the cross section is effectively velocity independent. For reference, for GeV dark matter with a typical velocity of 300 km/s and a silicon detector like XQC, $\sigma_{300} = 5.25 \times 10^{-21}\ \text{cm}^2$.

We reiterate in closing this subsection, that while the effective range parametrization can be used to characterize the cross section for any nuclear target A, there is no *a priori* relationship between the scattering length and effective range for different A values except if the Born approximation is valid.

C. Implication for experimental constraints

In the general spin-independent problem, the event rate per unit recoil energy is proportional to the differential cross section and one is interested in

$$\frac{dR}{dE_r} \sim \frac{d\sigma_A}{d\Omega}. \tag{24}$$

Here $d\sigma_A/d\Omega$ is the spin-independent DM-nucleus differential cross section for atomic mass A, $E_r = q^2/2m_A$ is the recoil energy and $q = 2\mu v \sin\frac{\theta}{2}$ is the momentum transfer, with θ being the center-of-mass scattering angle. Up until now, the Born approximation has been almost universally assumed for analyzing experimental limits.[5] When the Born approximation is valid, there are three distinct simplifications:

1. *Form factor and size of nucleus*

The difference between an extended source and a point-like source can be encoded in the form factor $F(q)$, defined by

---

[4] The standard notation "a" for scattering length used in this section should not be confused with the dimensionless parameter of the Schrödinger equation a introduced in Eq. (8).

[5] An exception is [17], which considered the possibility that DM resonant scattering could reconcile the DAMA and CDMS limits.

$$\frac{d\sigma}{d\Omega_{\mathrm{ext}}} \equiv \frac{d\sigma}{d\Omega_{pt}} F^2(q), \tag{25}$$

where $\vec{q}$ is the momentum transfer with magnitude q. The form factor carries the information about the charge distribution of the source. In a potential scattering problem, given the point source potential $V_{pt}(r)$ and the charge distribution $\rho(r)$ normalized as in Eq. (4), the potential of an extended source is determined by

$$V_{\mathrm{ext}}(\vec{r}) = \int V_{pt}(\vec{r} - \vec{r}')\rho(\vec{r}')d^3r'. \tag{26}$$

Given the potentials $V_{\mathrm{ext}}(r)$ and $V_{pt}(r)$ one can calculate the cross sections (at least numerically) and obtain the form factor $F(q)$ as the ratio of the two cross sections.

When first the Born approximation is valid, $F(q)$ is simply the Fourier transform of the charge distribution and is independent of the pointlike potential. Moreover, $F(q)$ goes to unity when the momentum transfer goes to zero: $F(0) = 1$. To see these properties, notice that the cross section in the first Born approximation is proportional to the Fourier transform of the potential,

$$\frac{d\sigma^{\mathrm{Born}}}{d\Omega} = \left| \frac{\mu}{2\pi} \int e^{i\vec{q}\cdot\vec{r}} V(\vec{r}) d^3r \right|^2. \tag{27}$$

Combining Eqs. (26) and (27), it is straightforward to show

$$\frac{d\sigma^{\mathrm{Born}}}{d\Omega_{\mathrm{ext}}} = \frac{d\sigma^{\mathrm{Born}}}{d\Omega_{pt}} \left| \int \rho(\vec{r}) e^{iq\cdot\vec{r}} d^3r \right|^2, \tag{28}$$

leading to the analytic expression for the form factor in the Born approximation,

$$F(q)^{\mathrm{Born}} = \int \rho(\vec{r}) e^{i\vec{q}\cdot\vec{r}} d^3r. \tag{29}$$

In practice, one measures the differential cross section experimentally as a function of q, divides it by the pointlike cross section in the Born approximation to obtain the form factor, and then does an inverse Fourier transform to get the charge distribution $\rho(r)$. This is how the charge distribution of the proton and some other light nuclei are determined from high-energy electron scattering [29]. For small momentum transfer $q \to 0$ or $qr_0 \ll 1$ where r_0 is the characteristic nuclear radius, the form factor is just unity,

$$F(0)^{\mathrm{Born}} = \int \rho(\vec{r}) d^3r = 1, \tag{30}$$

and the finite size of the nucleus does not influence the cross section,

$$\frac{d\sigma^{\mathrm{Born}}}{d\Omega_{\mathrm{ext}}} \approx \frac{d\sigma^{\mathrm{Born}}}{d\Omega_{pt}} \qquad (qr_0 \ll 1). \tag{31}$$

When the scattering is nonperturbative and the Born approximation is not valid, the form factor $F(q)$ cannot simply be determined by the charge distribution $\rho(r)$ as in Eq. (29). Furthermore, the form factor depends on the point-particle potential. In this case the form factor is not particularly useful and it is more straightforward to calculate the potential of an extended source based on an assumed charge distribution $\rho(r)$ as in Eq. (26), then calculate the cross section numerically by summing all partial waves we we do in this paper. If the point source potential is known, the calculated differential cross section can be compared to experimental results to see if $\rho(r)$ is a good model of charge distribution. Historically this method has been used to determine the charge distribution of heavy nuclei from high-energy electron scattering [30], where $Z\alpha_{\mathrm{EM}} \sim 1$ and the Born approximation is inaccurate. Modern methods also share the same spirit [31].

For small momentum transfer, we have to distinguish two cases in the nonperturbative regime. For a long range interaction like the Coulomb interaction, $F(0) = 1$ is still true even when the Born approximation is inaccurate. This follows from Gauss's law and is discussed in Ref. [31] for electron-Pb scattering both theoretically and experimentally. Measuring the form factor enabled the structure of the nucleus to be accurately determined once high-energy electrons (~100 MeV) became available in the 1950s; see Ref. [32] for a review. For a short range interaction with a massive mediator, $F(0) \neq 1$ in the nonperturbative regime, as can be seen in Fig. 7, where we have shown the exact form factor varies over nearly ten orders of magnitude for different atomic mass A. The difference of $F(q)$ in the low-energy limit for long range and short range interaction reflects the fact that Gauss's law is broken by a massive mediator. In classical electromagnetism with $1/r$ potential,

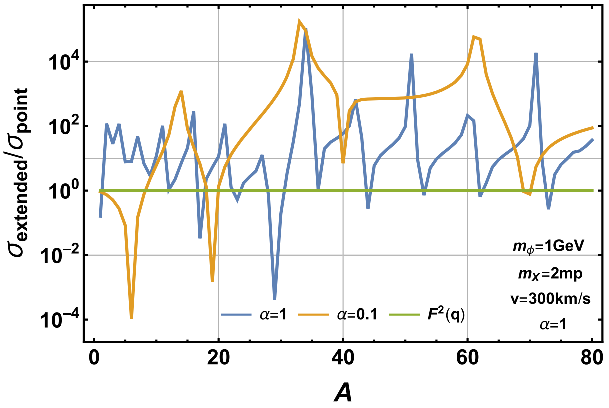

FIG. 7. $\sigma_A^{\mathrm{extended}}/\sigma_A^{\mathrm{point}}$, as a function of A, comparing to the Helm form factor $F_A^2(q)$ used, e.g., in [11], for the mean value of q given the scattering parameters. The Helm form factor is essentially 1 and incapable of accounting for the overall scaling of the cross section coming from the finite size of the nucleus. Additionally, for a heavier DM particle, q can be large and the corresponding wavelength can be smaller than the size of the nucleus, even in the low-energy regime, yet $F_A(q)$ is still inaccurate compared to the numerical calculation.

a extended charge distribution with total charge Q looks like a point charge Q from far away. This is not the case for a Yukawa potential.

The fact that $F(0)$ can differ from 1 contradicts a widely-held intuition from quantum mechanics that "when the de Broglie wavelength $(1/q)$ is much larger than the nuclear radius, the finite size of the nucleus does not matter." As our explicit calculations show, this intuition is not valid for a short range interaction in the nonperturbative regime. One way to understand this seeming paradox is through considering the attractive s-wave resonance described in Sec. II B 2. When the potential is strong enough to hold a negative-zero-energy s-wave bound state $(E = 0^-)$, low-energy scattering has a resonance with positive-zero energy $(E = 0^+)$. The wave functions of the loosely-bound $E = 0^-$ state and the soft scattering state $(E = 0^+)$ are actually indistinguishable [25]. Physically, this means that a low-energy incident particle with an infinitely long de Broglie wavelength nevertheless probes the inside of the potential well through the resonance and the zero-energy bound state. Since a pointlike Yukawa potential has a different bound state spectrum from the spectrum of an extended source, for the same α and m_ϕ, the structure of the source is reflected in the value of $F(0) \neq 1$.

This does not mean we can measure the nuclear structure with an arbitrarily low-energy incident particle (e.g., dark matter) when the de Broglie wavelength is much larger than the nuclear radius. At low energy, the differential cross section is isotropic and has no q dependence. All that can be measured is the magnitude of the cross section,

$$\frac{d\sigma}{d\Omega_{\rm ext}}(0) \propto \alpha^2 F^2(0). \tag{32}$$

Unless the fundamental coupling α has been determined from other measurements, the degeneracy between α and $F(0)$ cannot be eliminated and one cannot tell if $F(0)$ equals unity or not. Even if α is known and a low-energy scattering cross section is measured so that $F(0)$ is known and nonunity, we cannot determine the exact shape of the nuclear wave function from low-energy scattering alone, because different mass distribution may result in the same low-energy cross section and $F(0)$. All we can say is that the nucleus is not pointlike. More detailed information on the nuclear wave function requires a high-energy scattering experiment which can measure $F(q)$ as a function of q for some finite range of q.

In the analysis of weakly interacting massive particle (WIMP) direct detection in the literature (see [33] for example), dark matter is assumed to be weakly coupled so the Born approximation is valid. Then, the Born form factor Eq. (29) can be used. The nuclear charge distribution $\rho(r)$ can be measured through electron scattering experiments and the form factor obtained by Fourier transform. Among many different parametrizations, the Helm form factor [33,34] is most widely used; it satisfies $F(0)^{\rm Helm} = 1$ since it is derived from the Born approximation. Figure 7 shows that $F(0)^{\rm Helm}$ is extremely inaccurate for the nonperturbative scattering considered in this paper.

While our attention in this work is focused on small q where scattering is isotropic, we stress that even for the large q's encountered for massive DM and massive target nuclei, the Helm form factor is a poor approximation except for such weak coupling that the Born approximation is reliable. In general, the q dependence or angular dependence of the cross section must be determined by numerical calculation including higher partial waves.

2. Scaling of σ_A with A

The commonly-assumed Born approximation relationship between the DM-nucleus cross section in the Born approximation, $\sigma_A^{\rm Born}$, and the DM-nucleon cross section, σ_p, is

$$\sigma_A^{\rm Born} = \sigma_p \left(\frac{\mu_A}{\mu_p}\right)^2 A^2. \tag{33}$$

This can be obtained from Eq. (11) with $ab \ll 1$ or $\mu v \ll m_\phi$, i.e., in the low-energy regime compared to m_ϕ. When Eq. (33) is valid, as is the case for WIMP experiments [33], the final result of an experiment can be reported as a limit for σ_p. It is for this reason that different experiments and observations can put universal limits on σ_p to compare with each other, despite the fact that they are using different target nuclei. However the scaling relationship (33) between $\sigma_A^{\rm Born}$ and σ_p does not work in the resonant regime, as is shown in Fig. 8. In fact, the ratio σ_A/σ_p becomes highly parameter dependent. As a consequence, there is no universal rule to convert an experimental limit on σ_A to a single parameter σ_p, and it is

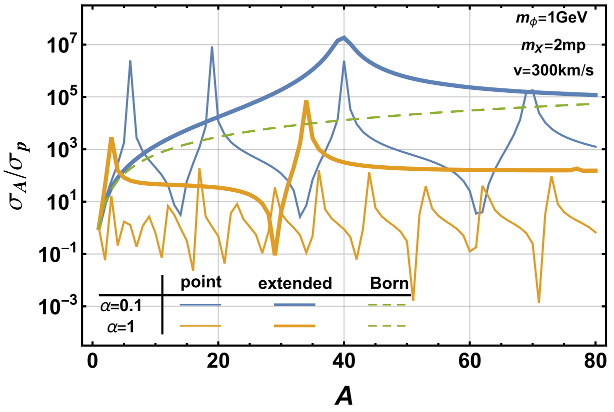

FIG. 8. σ_A/σ_p as a function of A. The green line is the Born approximation prediction (33), while blue and tan lines are the result of numerical calculation for point source and extended source, respectively. For an extended potential we take the nucleus radius as $r_A = A^{\frac{1}{3}}$ fm; in all cases the coupling is $\alpha_A = A\alpha$.

nontrivial to compare the results of different experiments. An additional complication is that experiments involving multiple materials with different A require an even more subtle study. In the following we provide the needed analysis, and obtain the correct inferences from the experiments and observations.

3. Connection to σ_p

In the absence of the Born approximation scaling relationship embodied in Eq. (33), the only way to relate σ_A to σ_p is to solve for both, under a given assumption for (α, m_X, m_ϕ). Neither σ_A nor σ_p are in general calculable perturbatively, and even for a pointlike proton, σ_p is not given by the simple Born approximation expression for it. In Fig. 9 we compare both pointlike and extended solutions of the Schrödinger equation to Born approximation for DM-proton scattering. Our extended model of the proton takes it to be a sphere of radius 1 fm (rms charge radius 0.77 fm) sourcing the Yukawa potential.

We have shown in Figs. 7–9 that the Born approximation fails badly in the quantum resonant regime, in all three respects—sensitivity to size, A dependence, and dependence of σ_p on fundamental parameters—so we must change the way the experiments are interpreted. We discard the form factor in our analysis and model the finite size of the nucleus with full numerical calculation for the extended Yukawa potential. We have already shown that in the quantum-resonant regime we are considering, the scattering is s-wave dominated and isotropic.

III. REINTERPRETING DIRECT DETECTION EXPERIMENTS

In this and the following section we derive the limits from various experiments and observations, focusing on the case of an attractive DM-nucleon interaction except where noted, for which the analysis is generally more subtle.

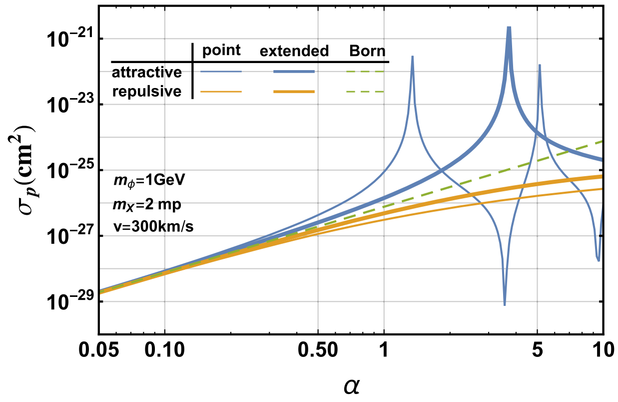

FIG. 9. σ_p as a function of α for the Born approximation, point source, and extended source. The Born approximation only holds for $\alpha \lesssim 0.3$, where the size of the nucleus and the sign of the potential do not matter.

A. The x-ray quantum calorimeter experiment

The x-ray quantum calorimeter (XQC) [35] was an experiment intended to measure the diffuse x-ray background using microcalorimeters on board a rocket sent to about 100 km altitude in the atmosphere. The results can also be used to put limits on the DM-nucleon cross section and extensive studies have been performed [10–12,36,37]. However these analyses uniformly used the nonvalid Born approximation to extract limits on σ_p, so in this section we reinterpret the latest analyses of XQC limits [11,12] as required to obtain reliable limits in the quantum resonant regime. The procedure is as follows:

(i) Rescale the limits reported for σ_p, back to the limits on the actual cross section that XQC is constraining—σ_{28}—undoing the assumed Born approximation scaling, (33). The XQC detector is actually made of silicon and a thin HgTe film, but the latter makes an insignificant contribution and we ignore it for simplicity. For DM mass ∼ few GeV, of special interest in connection with sexaquarks, the maximum momentum transfer is very small and the form factor $F(q)$ applied in [11,12] is essentially one. The dashed curve XQC (σ_{28}) in Fig. 1 shows the resultant limits on σ_{28}.

(ii) Using the numerical solution to the Yukawa potential model for extended nuclei, calculate σ_{28} everywhere in the parameter space (α, m_X, m_ϕ). We adopt $= R_0 A^{\frac{1}{3}}$, and calculate for $R_0 = 1.0$ and 1.2 fm to assess the sensitivity to the exact size of the nucleus. Comparing to the observational limit on σ_{28}, we then obtain the excluded region in (α, m_X, m_ϕ) shown in Fig. 10. Due to the resonant

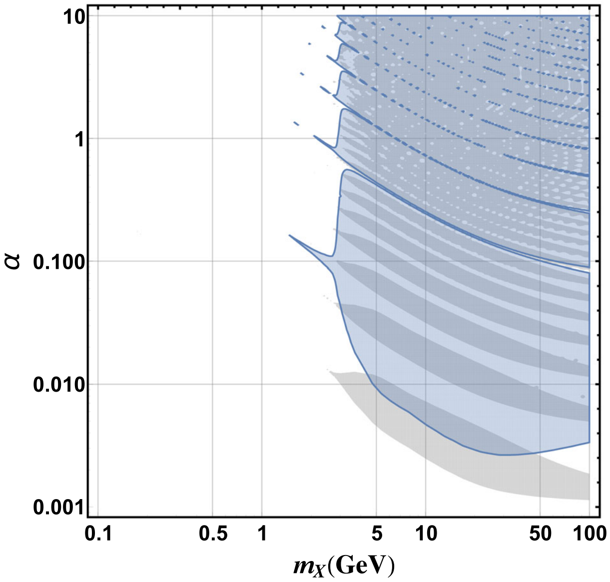

FIG. 10. Exclusion region in the (α,m_X) plane from XQC, for attractive point source (gray) and attractive extended source (blue) taking $R_0 = 1.0$ fm and $m_\phi = 1$ GeV.

behavior, the excluded/allowed regions of the parameter space has islands and holes whose exact positions depend on R_0.

(iii) Calculate σ_p for the allowed values of (α, m_X) to find the allowed region in the (σ_p, m_X) plane, for a given choice of m_ϕ. This enables a standardized comparison to other limits.

The procedure and its nontrivial character are illustrated in Fig. 11, which shows the exact and the Born predictions for σ_{28} and σ_p as a function of α, for $m_X = 2.9$ GeV and 10 GeV. Focusing first on the top panel, one sees how the nonperturbative cross section exceeds the Born approximation in some regions of α but is below it in others, and how important it is to take into account the extended nucleus properly. We return in Sec. V below to how these changes impact the XQC exclusion region in σ_p.

As noted in Sec. II B and illustrated in Fig. 6, the full, nonperturbative cross section has a nontrivial velocity dependence near a resonance, behaving as v^{-2} until saturating at some minimum velocity determined by the distance from resonance. We treat this nontrivial velocity dependence as follows. For XQC, we obtain a preliminary exclusion region evaluating σ_{28} at the characteristic DM velocity of $v = 300$ km/s and then check near the resonances whether a more accurate treatment is required. The maximum (escape) velocity for DM particles in the Milky Way halo is roughly $v \sim 600$ km/s. Thus near a resonance, the v^{-2} behavior of the cross section can result in a cross section as small as one-fourth of the value at 300 km/s. For $m_X \gtrsim 3$ GeV, this smaller cross section is still excluded by XQC because the basic XQC limit on the number of DM scattering events is so stringent. (For details, see [12].) This can be seen directly from the right panel of Fig. 11 for $m_X = 10$ GeV, where the XQC limit is usually more than three orders of magnitude smaller than the predicted cross section near the resonance. At still larger mass, DM can trigger the detector at velocities below 300 km/s with a equal or larger cross section than that at 300 km/s, so the spectrum-weighted event rate can potentially actually be higher than calculated using a constant $v = 300$ km/s value. In that case, the limits presented are conservative, as desired.

For smaller DM mass, $m_X \lesssim 3$ GeV, as shown in the left panel of Fig. 11, the XQC limit on σ_{28} is closer to the calculated cross section near or on resonance, and a factor-4 smaller cross section at $v \sim 600$ km/s could potentially

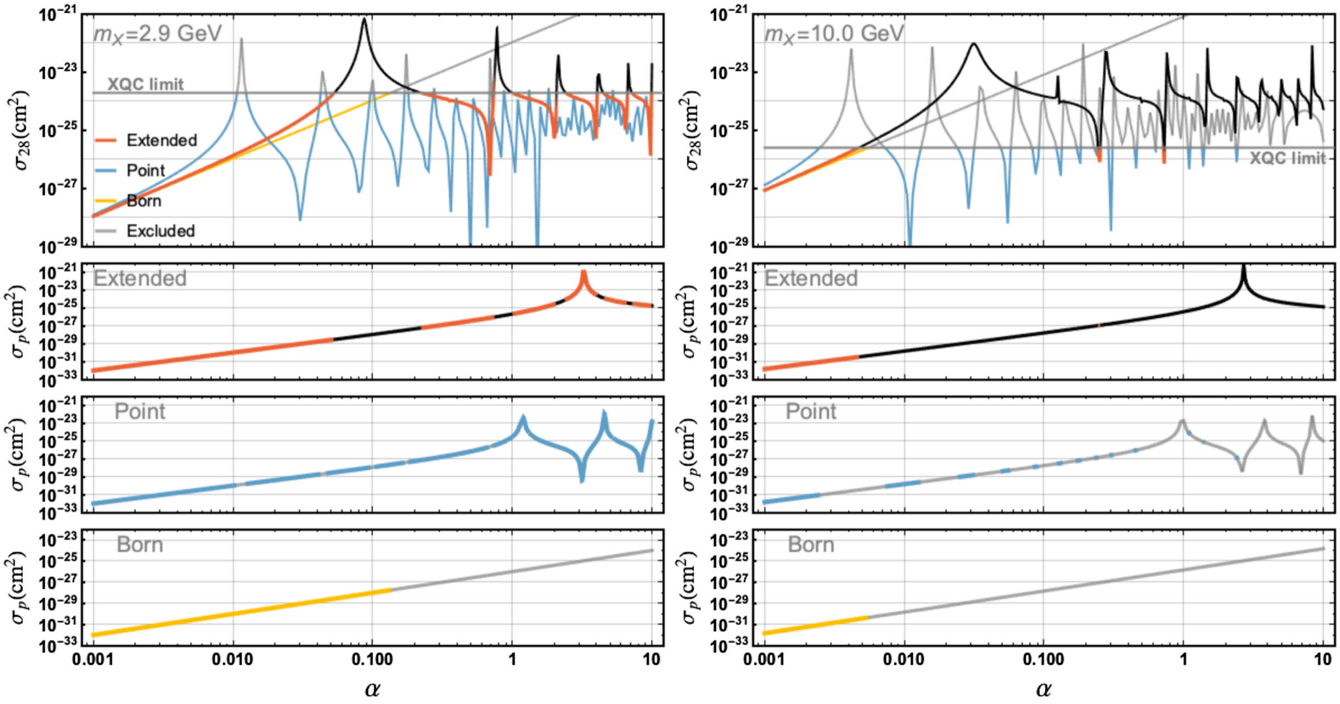

FIG. 11. The top panel shows σ_{28} versus α in the attractive case, for $m_X = 2.9$ GeV (left) and 10 GeV (right). The red/black lines show the exact treatment with extended nucleus, while cyan/gray and orange/gray show the results for point nucleus and the Born approximation. The gray horizontal line is the XQC limit on σ_{28}, so regions of α in which the predicted σ_{28} exceeds this limit are excluded and the curves are correspondingly shown in black or gray. The lower panels show, in the same color scheme, the corresponding σ_p predictions. The black regions are excluded; the gray regions would be excluded if the point Yukawa or Born approximations were applicable. This shows how an XQC upper limit on σ_{28} maps into excluded regions of σ_p, and illustrates how there can be "islands" of allowed and excluded parameters, unlike in the Born approximation or to a limited extent for the point Yukawa shown in the lower two rows.

evade the XQC limit. This would shrink the small blue peninsulas in Figs. 10, 12 (left), and 14 (left) for $m_X \lesssim 3$ GeV. However the peninsula is an uncertain region anyway due to its sensitivity to details of the nuclear wave function, which is not perfectly well-determined. Therefore we do not attempt a more refined analysis and simply leave the peninsula region unfilled in the cross section plots, to indicate the limit is uncertain.

B. The CRESST surface run experiment

The CRESST 2017 surface run took data using a cryogenic detector operated by the CRESST Collaboration [16,41,42] near ground level. The detector is made of Al_2O_3 and observed a total of 511 nuclear recoil events. It is shielded by ~30 cm of concrete in addition to the atmosphere of Earth. As a result, DM with large cross section in the overburden will loose too much energy to register in the detector. Roughly speaking, this places a maximum value on the cross section σ_p which can be probed in the CRESST surface run. Since the detector, the concrete and the atmosphere contain nuclei with different A, we modified the analysis done in [12], calculating each of the cross sections required in the analysis for any given set of parameters (α, m_ϕ, m_X). We thereby obtain the limits on the (α, m_X) parameter space shown in Fig. 12. The nontrivial character of the new exclusion limits is already evident in the emergence of a (narrow) excluded island which appears at large α for attractive interaction, from about $\alpha \approx 1$ at $m_X \approx 3$ GeV to $\alpha \approx 0.2$ at $m_X = 100$ GeV. This excluded band arises because even though the fundamental coupling is large, in this parameter regime the relevant nuclear scattering cross sections are small due to the existence of an antiresonance. In this region, DM can reach the CRESST detector with sufficient energy to be detected, while for larger and smaller parameter values it loses too much energy in the overburden.

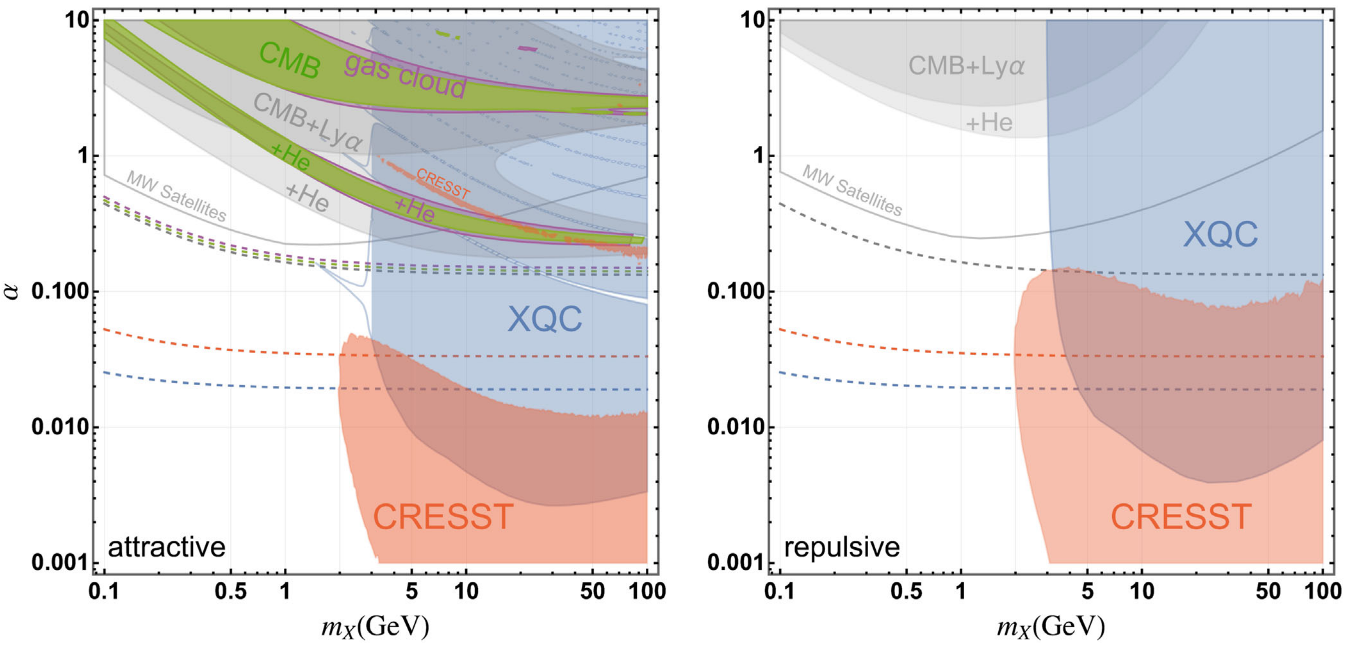

FIG. 12. Exclusion region in the (α, m_X) plane for $m_\phi = 1$ GeV, from XQC (blue) and CRESST (red), for attractive (left panel) and repulsive (right panel) interactions; the boundaries should be considered blurry because of their sensitivity to the details of the nuclear wave function. Note the narrow island of large α excluded by CRESST for $m_X \gtrsim 3$ GeV in the attractive case, thanks to antiresonance behavior in this regime. The secure limit from the CMB in the attractive case is shown in green, and the nearly-identical limit from gas clouds in purple. In each pair, the upper wider bands show the limit including only H, while the lower narrower stripes labeled "+He" are excluded due to the contribution of He. There are no corresponding CMB and gas cloud limits in the repulsive case, because there is no value of α giving a cross section large enough to saturate the bounds. If the limits based on combining CMB with Ly-α are trustworthy (see [38,39] for cautions), then the gray regions can be excluded using the results from [14], where the upper darker region includes H only and the lower lighter gray region is excluded by He in our nonperturbative analysis. In the left panel, for an attractive interaction, the unconstrained gap region above $m_X \approx 15$ GeV is due to an antiresonance in DM-He scattering. The gray solid line indicates the upper limits of α if the recent constraints based on Milky Way satellites [40] are validated. For each experiment or observation, the dashed line in the same color indicates the parameter values such that the dimensionless parameter b equals one; for $A = 4$ relevant for He in CMB, gas cloud, and Ly-α; $A = 16$ for O in CRESST; $A = 28$ (XQC). When $b \lesssim 1$ the Born approximation is reliable for the pointlike and extended Yukawa model, however unless $b \ll 1$ the extent of the nucleus still matters. If the interaction is repulsive (right panel), the boundary of XQC exclusion region is smooth due to the lack of resonance and there is no antiresonance contribution to the CRESST limit.

For CRESST, the lower exclusion region is close to the Born regime while the upper island for the attractive interaction is on antiresonance for most elements involved. Both regions are far from any resonance so that our treatment ignoring the velocity dependence near resonance is accurate.

IV. CMB AND ASTROPHYSICAL CONSTRAINTS

Another class of constraints, which extend to lower DM mass but are less powerful in terms of cross section limits than the direct detection experiments discussed in the previous section, derive from limits on heat exchange and friction between baryons and DM. The pioneering work of [7] showed that these effects from DM-baryon interactions suppress the cosmological growth of density contrast on small scales, so that precision data on the CMB power-spectrum constrains the DM-baryon cross section. A related but independent constraint comes from limits on heating of cold, dense and long-lived gas clouds in the Milky Way [43].

The CMB and gas clouds constraints have two features in common: (i) H and He are present in the cosmological abundance ratio, and (ii) the cross section values which can be constrained are in the nonperturbative regime, where Born scaling with A is not valid and finite size effects are important. As we shall see, the correct treatment significantly changes the derived limits. Two other systems have been proposed to probe structure growth on still smaller scales than accessed by the CMB power spectrum: Ly-α forest and dwarf satellites in the Milky Way. Using the reported Born approximation limits from [9,40], we provide the corresponding exact limits; if the constraints of [9,40] are established as robust, these will be stronger than the CMB and gas clouds limits.[6]

The observational constraints considered in this section bound a linear combination of $\sigma_{\rm H}$ and $\sigma_{\rm He}$, weighted by the H and He abundances and the energy- or momentum-transfer efficiency in a DM-nucleus collision. In the case of Milky Way gas clouds, higher-mass nuclei contribute as well. Analyzing using the Born approximation, as was done in previous analyses, implies assuming the fixed cross section ratio $\sigma_A^{\rm Born} = \sigma_p (\frac{\mu_A}{\mu_p})^2 A^2$. For instance for $m_X = \{2, 10\}$ GeV, $\sigma_{\rm He} = 16\frac{\mu_{\rm He}^2}{\mu_H^2}\sigma_H = \{66, 197\}\sigma_H$ [Eq. (33)]. Thus in the Born approximation He plays an important role, even though the He abundance is only ≈10% that of H, due to the large ratio of the Born cross sections. For high DM mass, the importance of heavier nuclei relative to protons is further enhanced by the higher-energy transfer efficiency in collisions of more nearly equal masses, with the average fraction of energy transferred to a slow-moving nucleus being $2m_A m_X/(m_A + m_X)^2$.

However in reality, for much of parameter space in the nonperturbative regime, $\sigma_{\rm He}$ is actually much smaller than the Born approximation estimate. The essential point is that to get cross sections at the barn level requires both strong coupling ($\alpha \approx \mathcal{O}(1)$) and being near a resonance value of α. But the resonances of H and He are at quite different values of α, so the H and He cross sections do not scale together as they do in the Born approximation. This is demonstrated in detail below.

A. Constraints from the CMB

DM interacting with baryons in the early Universe leaves an imprint on CMB observations, allowing limits on the cross section to be obtained [7–9]. We investigate the most recent results from [9] (Fig. 1) where both DM-hydrogen and DM-helium scattering are included. However [9] uses the Born approximation and assumes that only the proton interacts with DM in the initial calculation. It is clear now that any probes of the interaction of DM and baryons, with $A > 1$ in the nonperturbative regime, suffer from the problem of breaking down of the Born scaling (33). So a reinterpretation as done above for the XQC and CRESST experiments is necessary. Since the Yukawa cross section is velocity independent except near a resonant value of α, we begin by examining the $n = 0$ case treated in Sec. VII of [9]; in their notation $\sigma(v) = \sigma_0 (v/c)^{n=0}$.

In the early universe both DM-H ($A = 1$) and DM-He ($A = 4$) interactions are significant. What governs the limits on the cross section is the momentum transfer rate between DM and baryon fluids. Following the notation of [9] and starting from their Eq. (13),

$$\begin{aligned} R_X &= a c_0 \sum_i \frac{\rho_i \sigma_i v_i}{m_X + m_i} \\ &= \frac{a c_0 \rho_b v_H}{m_X + m_H} \sigma_H (1 - Y_{\rm He}) \\ &\quad \times \left(1 + \frac{Y_{\rm He}}{1 - Y_{\rm He}} \frac{\sigma_{\rm He}}{\sigma_H} \frac{v_{\rm He}}{v_H} \frac{m_X + m_H}{m_X + m_{\rm He}}\right), \end{aligned} \tag{34}$$

where a and c_0 are constants not relevant for us, the sum on i is the sum over all baryon species (here H and He), m_i is the nuclear mass, ρ_i is the density of nucleus i, and v_i and σ_i are, respectively, the average relative velocity and the scattering cross section between DM and baryon i; $Y_{\rm He} = 0.24$ is the helium mass fraction used by [9]. Defining σ_0 as the conservative limit on σ_H when $\sigma_{\rm He} = 0$, Ref. [9] reports σ_0 as a function of m_X. To include DM-He scattering, noticing that $v_{\rm He}/v_H = \sqrt{\mu_H/\mu_{\rm He}} \geq \frac{1}{2}$, we can write R_X as

---

[6] In a preliminary posting of this paper (arXiv:2101.00142v1 [44]) we only analyzed the CMB + Ly-α limits and did not consider the more robust but difficult-to-treat pure CMB limit. Here they are both given and shown separately in the figures, now also treating the repulsive case.

$$\begin{aligned} R_X &= \frac{ac_0\rho_b v_H}{m_X + m_H}\sigma_0(1 - Y_{\mathrm{He}}) \\ &= \frac{ac_0\rho_b v_H}{m_X + m_H}\sigma_H(1 - Y_{\mathrm{He}}) \\ &\quad\times\left(1 + \frac{Y_{\mathrm{He}}}{1 - Y_{\mathrm{He}}}\frac{\sigma_{\mathrm{He}}}{\sigma_H}\frac{v_{\mathrm{He}}}{v_H}\frac{m_X + m_H}{m_X + m_{\mathrm{He}}}\right) \\ &\geq \frac{ac_0\rho_b v_H}{m_X + m_H}\sigma_H(1 - Y_{\mathrm{He}}) \\ &\quad\times\left(1 + \frac{Y_{\mathrm{He}}}{1 - Y_{\mathrm{He}}}\frac{\sigma_{\mathrm{He}}}{\sigma_H}\frac{m_X + m_H}{2(m_X + m_{\mathrm{He}})}\right) \end{aligned} \tag{35}$$

which gives

$$\sigma_H + \left[\frac{Y_{\mathrm{He}}}{1 - Y_{\mathrm{He}}}\frac{m_X + m_H}{2(m_X + m_{\mathrm{He}})}\right]\sigma_{\mathrm{He}} \leq \sigma_0. \tag{36}$$

Depending on the assumed $\sigma_{\mathrm{He}}/\sigma_H$ one gets different limits on σ_H from σ_0, when σ_{He} is nonzero. The results of Ref. [9] were obtained using

$$\sigma_{\mathrm{He}} = 4\frac{\mu_{\mathrm{He}}^2}{\mu_H^2}\sigma_H, \tag{37}$$

corresponding to assuming DM only scatters on protons and not the neutrons in the helium, which is not appropriate if DM is an isoscalar as is the case for sexaquark DM and other nonphoton-mediated DM. Equation (37) also assumes the validity of Born approximation and thus breaks down in the quantum-resonant regime.

To place constraints on the Yukawa potential parameter space, we calculate (σ_{He}, σ_H) for a given choice of parameters (α, m_ϕ, m_X), then check whether the inequality Eq. (36) is violated.[7] We again model the proton as a solid sphere of radius 1 fm, since its rms charge radius ≈0.8 fm. Figure 12 shows the resultant exclusion region in (α, m_ϕ, m_X) in green, based on the m_X-dependent limit of [9] from the CMB temperature and polarization power spectra; e.g., $\sigma_0 < 6.3 \times 10^{-25}$ cm^2 for $m_X = 2$ GeV. For an attractive interaction, the narrow green band at lower α is where He is near resonance and the upper green exclusion region is where H is near resonance. There are also excluded "islands" at large α which are not shown.

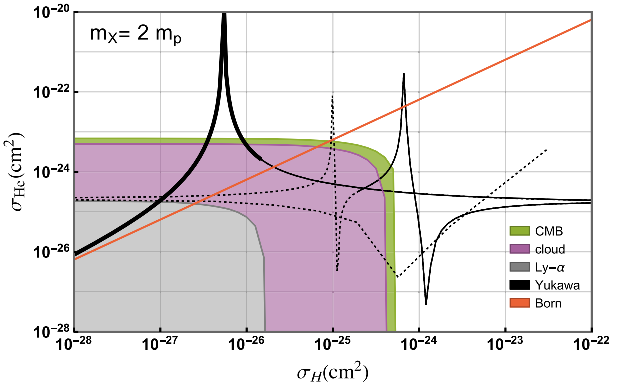

FIG. 13. The black line is the parametric curve of $\{\sigma_H, \sigma_{\mathrm{He}}\}$ for an attractive interaction and $m_X = 2m_p$, as a function of α, starting at the lower left (heavy line) α increases from 0.1 to 1; the medium line is for $1 < \alpha < 10$ and the dashed line for $10 < \alpha < 30$. The red line is the Born approximation relationship, $\sigma_{\mathrm{He}} = 16\frac{\mu_{\mathrm{He}}^2}{\mu_H^2}\sigma_H$, and the solid regions show the allowed domain from the CMB, gas clouds and CMB-Lyα.

It is instructive to identify the origin of the various excluded and allowed α ranges seen in Fig. 12 (left). Their origin can be understood by considering a parametric plot of $\sigma_{\mathrm{H}} - \sigma_{\mathrm{He}}$ as a function of α, shown in Fig. 13 for the case of $m_X = 2$ GeV. The colored regions in Fig. 13 show the allowed regions from various constraints. Following the thick black line from low α, He passes through a resonance for $0.6 < \alpha < 0.8$, producing the lower excluded band in Fig. 12 (left). For future reference, in this region $\sigma_H \approx 10^{-26.5}$ cm^2. As α increases further, neither cross section is large enough to violate the bound until H is close enough to resonance for $\alpha \approx 3$–5, that the gas clouds and CMB constraints are violated. Figure 13 also reveals an excluded region due to He for $\alpha \approx 15$. Importantly, for $\alpha \approx 25$ (the region of the antiresonance in H), $\sigma_H \approx 10^{-26.5}$ cm^2. This means that the lower excluded band in Fig. 12 (left) around $0.6 < \alpha < 0.8$ for $m_X = 2$ GeV, does not imply that the corresponding band around $\sigma_H \approx 10^{-26.5}$ cm^2 is excluded, because that same range of σ_H can be produced by an allowed (albeit large) α.

B. Potential constraints from Lyman-α forest and satellite dwarf galaxies

If the CMB + Lyman-α constraint of [9] is valid (questioned in [38]), the allowed region in Fig. 13 (applicable for an attractive interaction) is reduced to the gray domain; $\sigma_0 < 1.7 \times 10^{-26}$ cm^2 for $m_X = 2$ GeV. For small α, $\sigma_{\mathrm{He}}/\sigma_H$ is larger than given by the Born approximation, so the correct nonperturbative limit on σ_p is stronger than deduced using the Born approximation. At larger mass,

---

[7] Since the true DM-baryon cross section is velocity dependent near a resonance value of α for an attractive interaction, as discussed in Sec. II B, we evaluate ($\sigma_{\mathrm{He}}, \sigma_H$) at the typical relative velocity in the most constraining epoch for the CMB and CMB-Ly-α limits: $v_{\mathrm{CMB}} \approx 40$ km/s and $v_{\mathrm{Ly}\alpha} \approx 110$ km/s, respectively. These values can be inferred from the last two columns of Table I of [9], by solving for the velocities such that the $n = 0$ and $n = -2$ cross section limits are equal using the $m_X = 1$ GeV limits in that table. The v^{-2} velocity dependence only matters near the first resonance of σ_{He}, which are the "+He" regions in Fig. 12 (left). However, even for the maximum relative velocity $\sim 2v_{\mathrm{CMB}}$ (or $2v_{\mathrm{Ly}\alpha} \approx 110$ km/s) is used, σ_{He} would only be four times smaller, which is still well excluded. This can be seen from Fig. 13, where the σ_{He} peak is more than 10^3 times above the allowed region. Thus, our exclusion region is not modified by the velocity dependence, as a result of the strength of the constraints.

when $m_X \gtrsim 10$–15 GeV, another nonperturbative effect gives rise to a gap appearing in the CMB + Lyman-α limit for relatively large α due to He antiresonance regions in (α, m_ϕ, m_X), akin to those encountered in the XQC and CRESST analyses. We also note that stronger limit on DM-proton scattering cross section from Lyman-α forest was reported in Ref. [45]. If they are robust, the allowed cross section will be $\sigma_0 \lesssim 10^{-28}$ cm^2 for $m_X = 2$ GeV.

Interactions between DM and baryons which give rise to the cosmological CMB limits can also reveal themselves through suppression of low-mass dwarf galaxies [46]. This type of constraint must be considered less robust for now than the CMB constraints, since it relies on modeling nonlinear regime processes and is subject to uncertainties in interpreting dwarf galaxy observations. However since these limits may be put on a firmer footing in the future, we include the limits on (α, m_ϕ, m_X) using the constraints of [40] in Fig. 12, for reference.

C. Milky Way gas clouds

The limits on DM-baryon interactions from Milky Way gas clouds given in [43]—based on demanding that the heating/cooling rate of robust gas clouds due to scattering with DM particles not exceed the observed value—were derived assuming the Born approximation. However the Born approximation exaggerates the DM-nucleus cross sections for nuclei heavier than H even more than for He, and thus the analysis of [43] needs to be redone. The procedure to find σ_0 is similar to that discussed above for the CMB constraints and a relationship analogous to Eq. (36) can be obtained, now including contributions of nuclei heavier than He on the LHS of the inequality. In the nonperturbative regime we are considering, only H and He scattering make a significant contribution to heating/cooling, unlike in the analysis of [43] based on the Born approximation. For an attractive interaction, the exact nonperturbative treatment leads to the allowed region shown in Fig. 13, and the limits in the $\alpha - m_X$ plane shown in Fig. 12 (left).

V. COMBINED LIMITS ON THE DARK MATTER-NUCLEON INTERACTION

A. Attractive interaction

Combining the results from the previous section, we present our final limits on (α, m_X) and (σ_p, m_X) for $m_\phi = 1$ GeV and $R_0 = 1$ fm attractive interaction. The method of reinterpretation and analysis of experiments for repulsive interaction is the same and will be discussed second.

1. Limits on Yukawa parameter α

Figure 12 (left panel) shows the allowed and excluded regions of (α, m_X), for $m_\phi = 1$ GeV and $R_0 = 1$ fm, for an attractive interaction, applying constraints from XQC, CRESST, CMB, Lyman-α, and Milky Way satellites, and the astrophysical limits from gas cloud heating. The dashed lines indicate where $b = 1$, above which the interaction is strong enough that the Born approximation breaks down. Evidently, in much of the parameter space of interest we cannot trust the Born approximation, and in particular we cannot use the Born scaling (33) to draw our exclusion region, especially in the large coupling region probed by XQC and the CMB. The CRESST limit is almost always in the $b \lesssim 1$ region so we expect less deviation from the Born approximation and no resonances, except for the narrow antiresonance region in which CRESST has sensitivity for $\alpha \gtrsim 0.1$ for an attractive interaction.

There can be gaps in the exclusion from a single experiment due to resonant behavior of the cross section, such as for the CMB + Lyman-α constraints in Fig. 12 left. Moreover the exact positions of the gaps and boundaries move as the nuclear wave function and range of the Yukawa potential m_ϕ^{-1} are changed, so the positions of the boundaries should be considered blurry. Such gaps are generally better overcome by considering multiple experiments with different target mass number A, rather than trying to improve the sensitivity for the same experiment, since due to the nontrivial A-scaling in the resonant regime, different targets leave different gaps in the parameter space and the allowed region for one may be excluded for another.

2. Limits on σ_p

Figure 14 (left) shows the updated DM-proton cross section limits from our analysis of XQC, CRESST, and gas clouds, as well as the cosmology-based constraints. The previous state-of-the-art limits are shown as dashed lines from XQC [11,12], CRESST [12], CMB, and CMB + Lyα [9], and gas clouds [43]. The derivation of our limits are discussed below in turn.

Starting with XQC, in [11,12] it was assessed based on the Born approximation that XQC had sensitivity to proton cross sections $\gtrsim$1 mb for $m_X \leq 3$ GeV, via multiple scattering of a single DM particle in the detector allowing sufficient total energy deposit to meet the threshold condition. (The relevance of multiple scattering for low masses was first pointed out in [10].) However this apparent sensitivity disappears in our more accurate treatment, as can be understood from Fig. 11. The salient points are that:

1. The XQC upper limit on σ_{28} becomes weaker and weaker for lighter DM, because a larger and larger number of multiple scatterings in the detector are needed to produce a total energy deposit above threshold.
2. For light DM requiring multiple scattering, e.g., $m_X = 2.9$ GeV shown in the left panel of Fig. 11, $\sigma_{28}^{\rm Born} > \sigma_{28}^{\rm Exact}$ for $\alpha > 0.2$. Therefore, in this regime the Born approximation exaggerates the ability to exclude. In the narrow region around $\alpha \approx 0.1$, the opposite is true, resulting in an actually-excluded

"peninsula" around $\sigma_p \approx 10^{-28}$ cm^2, which is not evident from the Born approximation. If we calculate to a larger $\alpha > 10$, allowed α for σ_{28} near a DM-proton antiresonance could potentially produce σ_p values in the "peninsula," reducing its size. However the position and extent of this excluded peninsula is not in any case well-determined, due to nuclear wave function sensitivity and our crude treatment of the velocity dependence for that part of the analysis, as discussed in Sec. III A.

(3) At higher mass, e.g., $m_X = 10$ GeV shown in the right panel of Fig. 11, the more stringent limit on σ_{28} requires α to be so small it is barely out of the Born regime and the treatment of [11,12] is fairly accurate. However, since the exact σ_{28} is larger than the Born value for α in this regime, the XQC limit is strengthened when the exact treatment is used. Allowing higher $\alpha > 10$ will not make any difference because all $\alpha > 10$ are excluded due to the strong constraint on σ_{28}: no antiresonance can make σ_{28} small enough to evade the limit.

For CRESST, comparing the new limits given by the shaded regions to the old dashed limits in Fig. 14, we see that the true sensitivity region is generally reduced compared to what the perturbative analysis indicated, except for a sliver which appears at higher cross section. The loss in CRESST's sensitivity to cross-sections $\sim 10^{-29}$ cm^2 falls in the XQC-excluded region, except for 2 GeV $< m_X <$ 3 GeV.

According to our exact results, the limits from CMB alone (green solid in Fig. 14) are considerably weaker than given by [9] (green dashed in Fig. 14). This is because [9] assumes a $4(\mu_{\rm He}/\mu_H)^2$ times larger cross section on He than on H, whereas in fact the He cross section is negligible for α large enough to produce a σ_p at the limit. The green dotted "+He" region appears to exclude a range of cross sections allowed by the Born approximation analysis (the old dashed limit). In this region, the Born approximation underestimates the true He contribution which is larger than Born due to a DM-He resonance. However, allowing a larger α up to ~ 30 enables σ_p to take these values due to an allowed H antiresonance as shown in Fig. 13. The gap between the confidently excluded solid region and the

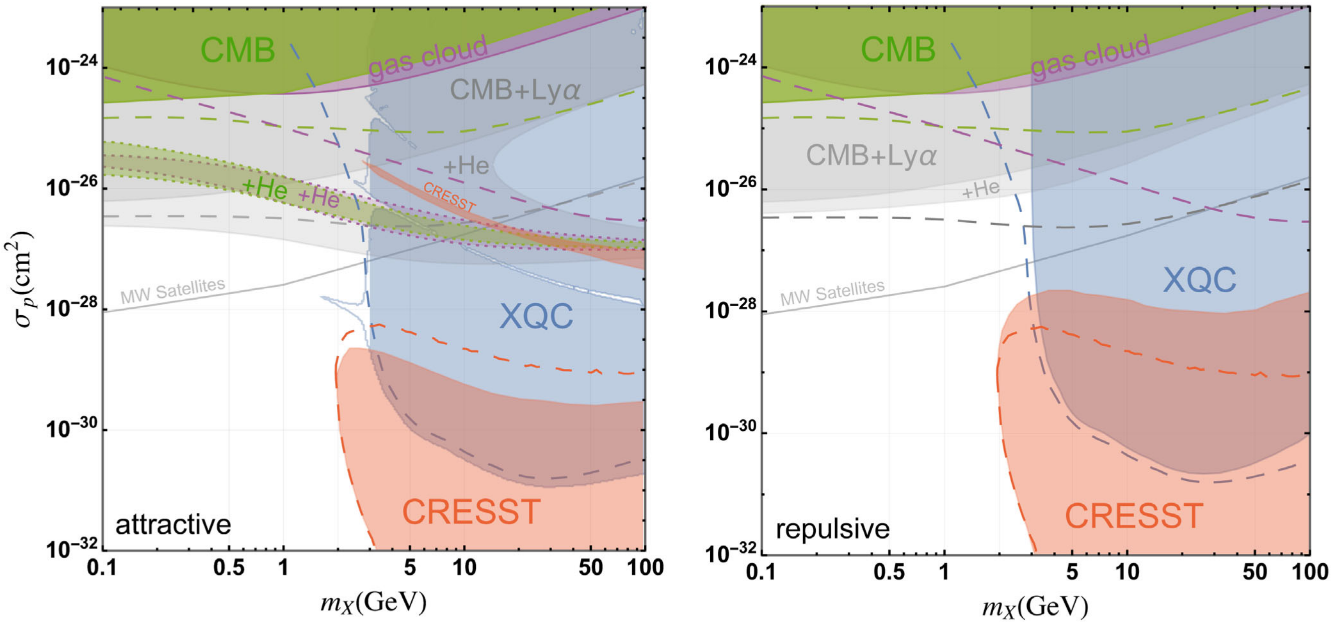

FIG. 14. Exclusion region in (σ_p,m_X) space from various constraints for attractive (left panel) and repulsive (right panel) interactions, for $m_\phi = 1$ GeV. Above $m_X \approx 3$ GeV the strongest limits come from direct detection experiments, XQC in blue and CRESST in red. For low masses, the strongest unambiguous limit is from CMB constraints on structure formation, shown as the green region labeled "CMB." Astrophysical limits from gas cloud cooling, shown in purple, provide the strongest constraint in the 1–3 GeV range. For anattractive interaction, the green and purple bands surrounded by dotted lines and labeled "+He" are actually not fully excluded in the nonperturbative treatment if larger coupling α is allowed as discussed in Sec. IV A, but if a theoretical limit of $\alpha < \mathcal{O}(1)$ is imposed these bands are excluded. For repulsive interaction, the CMB (green) and gas cloud (purple) limits cannot place any constraint on the (α, m_X) parameter space, including DM-He scattering or not. So we only plot the unambiguous DM-proton scattering limits without reinterpretation. The gray regions labeled "CMB + Lyα," "+He" and gray line for "MW Satellites" are based on constraints which may not be robust and are included just for reference, as discussed in Sec. IV B. The heavy dashed lines in the corresponding color show the previous Born-approximation-based limits. [The original CMB and Lyman-α limits (green and gray, dashed) have been modified slightly by changing the numerical factor in Eq. (37) for He from 4 to 16 to include both proton and neutron scattering, as appropriate for isoscalar DM.].

ambiguous dotted region is where the DM-He cross section is small and He contribution is negligible. The situation is the same for the gas cloud limit as the CMB limits, with just minor differences in the shapes of the exclusion regions and similar potential for large-α antiresonance to produce nonexcluded σ_p in this range.

If the CMB + Lyα limits can be used, the light gray region due to He scattering will only shrink a bit and not disappear completely if larger α are allowed, simply because the limit from Ly-α is stronger and the allowed α range is much smaller in the (α, m_X) plane. A large gap in the limits appears for $m_X \geq 10$ GeV due to He antiresonance, which is, however, closed by XQC. Comparing to the limit obtained with only proton scattering, including helium results in a stronger limit in general except in the gap caused by the small DM-He cross section near He antiresonance, and allowing a larger α could reduce or eliminate the contribution of He.

If reliable, the Milky Way satellites limit for DM-proton scattering [40] would be stronger than the CMB + Lyα limit, for $m_X \lesssim 10$ GeV. It is weaker for heavier DM when He scattering is included, although it would close part of the gap in the CMB + Lyα limit. The underlying source of the satellites limit is inhibition of small-scale structure formation from DM-baryon interactions, similarly to the CMB limits. The limit relies on the validity of the mapping from linear-regime structure to as-observed dwarf galaxies used in [40], based on LCDM simulations which may not adequately describe interacting DM among other issues so its robustness needs further investigation.

B. Repulsive interaction

Since the sign of the DM-ϕ coupling is unknown, in this subsection we repeat the analysis for a repulsive interaction with $\alpha \to -\alpha$ in Eq. (1). A repulsive potential does not allow the formation of bound states, so there is no resonance or antiresonance for the cross section. At low energy the scattering is still s-wave dominated, and $\sigma \sim v^0$, i.e., no special velocity dependence. However, as for the attractive interaction, the Born approximation breaks down when α (or the dimensionless parameter b) is large. This is clearly shown in Fig. 9. Most of the nonperturbative effects appearing in the analysis for attractive interaction still apply for the repulsive case. In particular, the nontrivial A dependence still persists and reinterpretation of constraints involving $A > 1$ is needed.

The maximum value of the cross section that can be achieved with a repulsive interaction is also different from the attractive case. For an attractive interaction, the maximum cross section is achieved at the s-wave resonance, where the phase shift is close to $\pi/2$ and the cross section saturates the unitarity bound given in Eq. (13),

$$\sigma = 4\pi/(\mu v)^2. \tag{38}$$

For Galactic dark matter with $v \gtrsim 100$ km/s and GeV-scale mass, $\sigma \lesssim 10^{-21}$ cm^3 on resonance. The CMB limit as shown in Fig. 1 is strong enough to constrain such resonant values. However, for the repulsive case, without the resonance, the cross section is bounded by the range of the interaction. When the radius of the nucleus is much larger than the Compton wavelength of the mediator, $r_A \gg 1/m_\phi$, the limit is given by the geometrical size of the nucleus, $\sigma_A \lesssim 4\pi r_A^2$. This is seen in Ref. [15], where a repulsive finite square well potential is used. The corresponding limit in the extended Yukawa potential (6) is $r_A m_\phi \to \infty$. For a proton, $r_\mathrm{H} \sim$ fm and the cross section caps at $\sigma_\mathrm{H} \sim 10^{-25}$ cm^2. With the maximum possible σ_H being smaller than the CMB limits, the repulsive parameter space is unconstrained by these limits. This roughly applies for our benchmark $m_\phi \sim$ GeV. For a lighter mediator, the cross section is determined by $1/m_\phi$ rather than r_A and could be greater than the CMB limit. Reference [15] also discussed another possibility for the cross section to exceed the size of nucleus, so that the CMB limit can be relevant; when the dark matter particle itself is not pointlike, in which case the cross section can be as large as the size of the DM particle instead of the nucleus. A followup experimental analysis [47] places corresponding limits on nonpointlike dark matter.

1. Limits on Yukawa parameter α

Figure 12 (right) shows the constraints in the (α, m_X) plane for a repulsive interaction. There are several differences from its attractive counterpart. The XQC boundary gets smoothed out and no gap is formed, because of the lack of (anti)resonance. The cross section depends monotonically on the underlying parameters so no gaps appear in the excluded domain. The upper reach of CRESST is increased because the repulsive interaction has a generally smaller cross section so the overburden produces less shielding the antiresonance excluded band at large alpha also disappears. The CMB limit disappears entirely due to the inability to saturate the cross section limit for the repulsive interaction, as discussed previously. Actually, detailed calculation shows that for $m_\phi = 1$ GeV, the CMB limit is only sensitive in the repulsive case to $\alpha \gtrsim 10^3$ for $m_X =$ 1 GeV and $\alpha \gtrsim 10^8$ for $m_X = 10$ GeV, and the contribution from DM-He scattering is ignorable. The gas cloud limit is similar to the CMB one and also does not contribute to the constraint on (α, m_X). The CMB + Lyman-α limit, if reliable, would be much stronger than the CMB-only limit and including DM-He scattering would improve the bound; however there is no gap like the one seen in the left panel for the attractive case.

2. Limits on σ_p

Figure 14 (right) shows the exclusion region for (σ_p, m_X) for a repulsive interaction. The boundary of the XQC excluded region is smoothed and the upper reach of CRESST is increased. The green CMB limit and cyan gas cloud limit are the original constraints including only proton scattering and are what we can safely trust without reinterpretation. In general, the repulsive interaction cannot achieve these cross sections, or even if it does, with extremely large α, the contribution of He and heavier nuclei can be ignored because they have similar geometrical size as the proton but are significantly less abundant. If the CMB + Lyman-α limit can be used, including He does improve the constraint, albeit not as much as with the (invalid) Born approximation prescription, because $\sigma_{\mathrm{He}}/\sigma_{\mathrm{H}}$ is much smaller than the Born scaling [Eq. (33)].

C. Dependence on mediator mass

We adopted $m_\phi = 1$ GeV for our analysis, to be concrete and because for sexaquark DM the dominant interaction with nucleons is through exchange of the flavor-singlet combination of $\omega - \phi$ vector mesons, whose mass is in this range. For heavier-than-GeV m_ϕ, and for heavy target nuclei such as Si in XQC and the majority of nuclei in CRESST, the condition $r_A \gg 1/m_\phi$ is well-satisfied and the scattering potential can be approximated by a uniform spherical well with radius r_A and depth $V_0 \propto \alpha/m_\phi^2$, as indicated in Eq. (7). In this case, the scattering cross section for a given nucleus is only a function of α/m_ϕ^2. As a result, our exclusion region in Fig. 12 is the same for a different m_ϕ, except for a rescaling of the α-axis by the factor $\alpha \sim m_\phi^2$. Returning to the limits on the scattering cross section for a given nucleus undoes this rescaling, with the result that the limits in Fig. 14 remain the same for any $m_\phi > 1$ GeV.

For lighter nuclei such as H and He and for lighter $m_\phi \lesssim 100$ MeV, we have $r_A \lesssim 1/m_\phi$ and the potential deviates from being a spherical well. The cross sections cannot be obtained by any simple rescaling of the $m_\phi \sim$ GeV result and need to be re-calculated. However, there are still some simplifications for light m_ϕ:

(1) For $m_\phi \lesssim 10$ MeV, we have $r_A \ll 1/m_\phi$ or $c/b \ll 1$ and the point Yukawa potential Eq. (1) is enough. The size of the nucleus does not matter.

(2) For $m_\phi \sim (0.1\text{–}1)$ MeV the Born approximation Eq. (11) turns out to be quite accurate for $\sigma_p \lesssim 10^{-21}$ cm^2. However the oft-used "Born scaling" to trivially relate cross sections for different A using Eq. (33) is still wrong in this case, since we do not have $\mu v \ll m_\phi$ or $ab \ll 1$ now. The full Born approximation Eq. (11) should be used.

(3) For $m_\phi \lesssim 0.1$ MeV, we have $ab \gg 1$ which enters into the classical regime and there is no resonance (see Fig. 2). The classical problem has been solved and a fitting function was given in Ref. [24,48],

$$\sigma_T \approx \begin{cases} \frac{4\pi}{m_\phi^2}\beta^2 \ln(1+\beta^{-1}), & \beta \lesssim 0.1 \\ \frac{8\pi}{m_\phi^2}\beta^2/(1+1.5\beta^{1.65}), & 0.1 \lesssim \beta \lesssim 10^3, \\ \frac{\pi}{m_\phi^2}(\ln\beta + 1 - \frac{1}{2}\ln^{-1}\beta)^2 & \beta \geq 10^3 \end{cases} \quad (39)$$

where $\beta = \alpha m_\phi/(\mu v^2)$. Notice here many partial waves contribute and the momentum transfer cross section has to be used to ensure convergence.

We include Fig. 18 in the Appendix C to show the limits on $(\sigma_p,\ m_X)$ for $m_\phi = (1, 10, 100)$ MeV for completeness. Cross sections for $m_\phi \lesssim 1$ MeV can be calculated analytically using the Born approximation or classical fitting function as described above.

D. The interpretation of a DM-baryon cross section exceeding 10^{-25} cm^2

Regardless of whether the DM is pointlike or composite, the DM-baryon cross section can exceed 10^{-25} cm^2, contrary to statements in the literature.[8] This can be seen both in our explicit calculations and from partial wave unitarity. Unitarity gives the maximum s-wave cross section [cf. Eqs. (13) and (A4)]

$$\sigma_{\mathrm{peak}} = \frac{4\pi}{\mu^2 v^2} = 4.9 \times 10^{-21}\ \mathrm{cm}^2 \left(\frac{\mathrm{GeV}}{\mu}\frac{10^{-3}c}{v}\right)^2, \quad (40)$$

where μ is the reduced mass and v is the relative velocity. The unitarity-limit cross section is reached when the parameters of the DM-nucleus or DM-nucleon potential are such that the system has a zero-energy bound state; this can occur whether or not the DM particle is pointlike. Note that the s-wave unitarity limit is the same whether the particles scattering are pointlike or extended [Eq. (A4)]. Figure 9 shows σ_p for a pointlike DM particle and both a point and extended nucleon as a function of α, for $(m_X, m_\phi) = (2m_p, 1\ \mathrm{GeV})$ and relative velocity 300 km/s. The peak cross sections occur at different values of α for the pointlike and extended nucleon cases, but in both instances they reach the same unitarity limit value given above; $10^{-20.3}$ cm^2 for $v = 300$ km/s. (The apparent difference in

---

[8] E.g., Ref. [15] in the conclusion; "(3) For $\sigma_{\chi N} > 10^{-25}$ cm^2, dark matter cannot be pointlike. Contact interactions cannot achieve cross sections larger than the geometric cross section $\sigma_{\chi A} = 4\pi r_A^2$, and simple light mediators are strongly ruled out. Dark matter with cross sections in this range must be composite." See also Ref. [47], e.g., in the abstract; "Recently, it was shown theoretically that the scattering cross section for $m_\chi \gtrsim 1$ GeV pointlike dark matter with a nucleus cannot be significantly larger than the geometric cross section of the nucleus. This realization closes the parameter space for pointlike strongly interacting dark matter." *Note added, September 2022:* We understand that an erratum is being prepared for Ref. [15] to correct this misstatement ([49]).

peak heights in Fig. 9 is due to the discretization of the plotting function.)

Whether or not the unitarity bound can be saturated depends on whether the interaction is repulsive or attractive. The existence of resonances and the possibility of near saturation of unitarity is a very general feature of attractive potentials. In the case of a Yukawa sourced by a nucleus, the particular coupling strength giving rise to a resonance depends on the mass of the mediator and the size and shape of the source. For a fixed coupling strength and mediator mass, how close the cross section comes to saturating unitarity depends on the nuclear size A. Using another nuclear wave function than a simple sphere would also shift the parameter values of the resonance. However the existence of a near-resonance is generic, as long as a near-zero-energy bound state exists for some A given the fundamental parameters. This leads to large cross sections with the velocity dependence discussed in Sec. B. However if the potential is repulsive it does not admit zero-energy bound states and unitarity is not saturated. The maximum cross section for pointlike DM in the repulsive case is therefore more limited, as discussed in Sec. V B. With a mediator no lighter than a pion, the cross section can only reach $10^{-24.1}$ cm^2.

The possibility of using the magnitude of the DM-nucleus cross section as a diagnostic of dark sector particles having extended structure is certainly tantalizing. If the distribution of μv for the DM were known and the cross section were established to exceed the s-wave unitarity limit, that would be evidence of multiple partial waves contributing simultaneously and suggest the de Broglie wavelength $1/\mu v$ is smaller than the length scale in the scattering system. This scale can be the size of the nucleus, the size of the DM particle, or the Compton wavelength of the mediator $1/m_\phi$, whichever is the largest. A detailed analysis would be required to decide. Measuring the cross section for a variety of nuclei A would be a valuable diagnostic. Constraints on light mediator candidates and m_ϕ could also help narrow down the possibilities [15].

VI. FINAL JOINT LIMITS AND CONCLUSIONS

We have shown that the pioneering and state-of-the-art analyses of direct detection and CMB and astrophysical constraints are not generally valid due to inappropriate use of the Born approximation to relate the cross sections for nuclei of different A to that of protons. Furthermore, earlier analyses did not properly take into account the finite size of nuclei.

DM-baryon elastic scattering via a massive mediator in general exhibits resonance behavior if the interaction is attractive and can depart significantly from the Born approximation result even for repulsive interactions. Thus DM interactions with baryons must be analyzed by exact numerical solution of the Schrödinger equation in a substantial portion of interesting parameter space. For example, GeV-range dark matter with an attractive Yukawa interaction lies in the nonperturbative resonant regime for the XQC experiment with $A = 28$, even for Yukawa coupling strength as low as $\alpha = 0.02$.

In the resonant regime, it is nontrivial to interpret results of direct detection experiments and other constraints from observations, particularly when $A > 1$ nuclei are used as targets. Universal limits on the DM-nucleon cross section cannot be directly obtained as long as it is the DM-A cross section that is actually experimentally constrained, since there is a nontrivial, model-dependent relationship between σ_p and σ_A. For example, XQC using a silicon detector leaves a large part of $(\sigma_p,\, m_X)$ parameter space for $m_X \lesssim$ 3 GeV allowed, rather than being excluded as concluded previously based on naive use of the Born approximation.

Analyses of CMB constraints also need modification, due to the nontrivial relation between DM-He and DM-p cross sections. When this is taken into account, the CMB limits are weakened because large σ_p does not imply large σ_{He} or vice-versa. If the CMB + Ly-α constraints are valid (which is not yet clear, given current limited understanding of patchy reionization [38,39]), they would strengthen the limits relative to CMB-only limits but still leave a gap in the exclusion region for relatively large coupling, due to antiresonance behavior which sharply reduces the DM-He cross-section for DM mass above 10–15 GeV. At the same time, the correct treatment strengthens CMB + Ly-α limits for lower masses and smaller σ_p, due to the nonperturbative enhancement of σ_{He} in this parameter regime. A further strengthening of the limits would be possible if the Milky Way satellites analysis proves robust, as shown in Fig. 14.

Our summary results on the excluded regions for the Yukawa coupling and DM-nucleon cross section are shown in Figs. 12 and 14 for the attractive and repulsive cases separately. Figure 15 combines these results and gives the final constraints which can be placed today on (σ_p, m_X) using XQC, CRESST, CMB, and Gas Clouds, if the sign of the Yukawa coupling is unknown. Even the step of combining the limits presents a nuance. A plot could usefully aim to address two different questions: (1) Can the data from a given experiment exclude a given point in (σ_p, m_X), independent of the sign of the interaction? or (2) Is a given point in (σ_p, m_X) inconsistent with all experiments sensitive to that m_X? The excluded region of type (1) for a particular experiment is the intersection of the excluded regions in the left and right panels of Fig. 14 for the same experiment. These experiment-by-experiment fully-excluded regions are shown using solid colors in Fig. 15, for each of the robust constraints: CMB, gas clouds, XQC and CRESST.

Additionally, Fig. 15 shows how the exclusion region increases for each experiment if the sign were *a priori* known, using solid for an attractive interaction and dashed for repulsive. The intersection of the XQC and CRESST

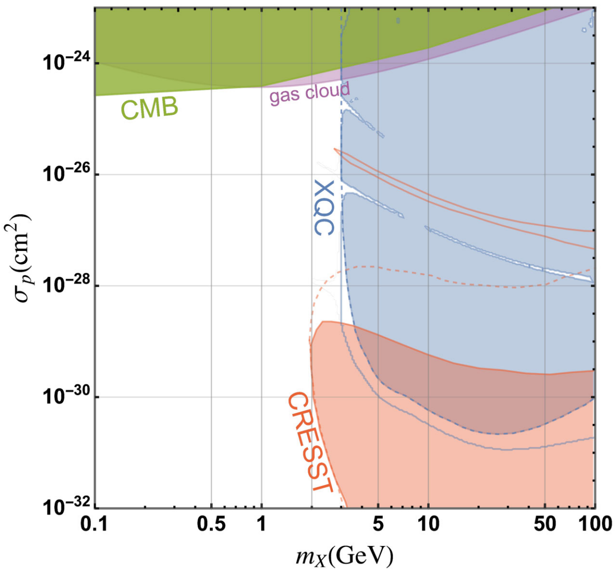

FIG. 15. The final exclusion regions for σ_p as a function of m_X, for $m_\phi = 1$ GeV, adopting the more conservative assumption on the sign of the interaction for each parameter combination and not including CMB + Ly-α and Milky Way satellites constraints which may not be robust. The XQC limits are more conservative (weaker) for the repulsive case, while the CRESST exclusion region is a mix. The island at large cross section which is excluded if the interaction is attractive, due to the antiresonance in that case, is allowed for a repulsive interaction and thus cannot be excluded in the absence of knowledge of the sign. Similarly, the conservative choice for the lower excluded region is for the attractive sign since it extends to higher cross section if the interaction is repulsive. For $m_X \lesssim 2$ GeV and $\sigma_p \lesssim \text{few} \times 10^{-25}$ cm^2 the parameter space remains unconstrained. Measuring the thermalization efficiency of XQC to determine the accurate m_X value of its lower reach is very important.

solid regions is even more robustly excluded than the nonoverlapping regions, due to having independent experiments giving the same conclusion. However the wedge bounded by blue solid and blue dashed lines, and red solid and red dashed lines, [containing $(\sigma_p, m_X) \approx (10^{-28}\ \mathrm{cm}^2, 3\ \mathrm{GeV})$], is not excluded by both experiments because it is excluded by XQC only if the interaction is attractive, and by CRESST only if it is repulsive.

The interesting parameter space for sexaquark DM ($m_X \lesssim 2$ GeV) remains largely unconstrained, requiring only $\sigma_p \lesssim 10^{-24.5}$ cm^2. The constraints on the Yukawa coupling parameter are quite limited for DM mass below XQC sensitivity, $m_X \lesssim 3$ GeV, with only small ranges of α being excluded. If Ly-α measurements can be used to constrain the growth of small scale structure, $\alpha \gtrsim 0.3$ could be excluded for attractive interaction and $m_X \approx 2$ GeV, leading to an upper limit on the cross section in the mb range. That would be constraining but not challenging for sexaquark DM. The constraints are stronger for heavier DM, where the energy deposit per collision is larger and the direct detection experiments XQC and CRESST are more sensitive. As pointed out in [6,12], it is crucial to measure the thermalization efficiency of semiconductors to small nuclear recoils before experiments like XQC can be interpreted for lower DM masses. It should also be noted that if the thermalization efficiency is smaller than the 0.01 adopted here, as may be the case, the limits should be weaker than indicated and those indicated in the plot would not be conservative.

Recently, in Ref. [50] the authors performed experiments with 27 different atomic nuclei and reported limits on σ_{DM-A} for each of them, extending the limits of Ref. [51] derived by consideration of the atmosphere of DM particles surrounding the Earth and its impact on the evaporation of cryogens and drag on the Hubble space telescope. Due to the complexity of the analysis, we leave consideration of [50,51] for elsewhere. However the combination of the lower mass reach and large coverage in A of the constraints of [50,51], offers promise that these will be a valuable addition to the constraints on DM interactions with hadrons, for DM in the GeV mass range.[9]

ACKNOWLEDGMENTS

We thank M. S. Mahdawi for discussions, and for the use of his code developed for the studies reported in [11,12], and thank J. F. Beacom and C. V. Cappiello for helpful comments and discussions about the manuscript. X. X. received support from a James Arthur Graduate Fellowship; the research of G. R. F. has been supported in part by the Simons Foundation and by Grants No. NSF-PHY-1517319 and No. NSF-PHY-2013199.

APPENDIX A: NUMERICAL METHODS

To obtain the total elastic scattering cross section for DM-baryon scattering in the nonrelativistic regime, we need to solve the Schrödinger equation exactly with the appropriate point or extended Yukawa potential and perform a partial wave analysis. Two approaches are discussed below; which is superior depends on regime.

1. Schrödinger equation method

In the first approach, we follow the method described in [22,53]. Although that work addresses the collision between DM particles, the mathematical problem is exactly the same. The radial Schrödinger equation in this problem is

$$\left\{\frac{1}{r^2}\frac{d}{dr}\left(r^2\frac{d}{dr}\right)+k^2-\frac{l(l+1)}{r^2}-2\mu V(r)\right\}R_l(r)=0 \quad \text{(A1)}$$

---

[9] Since the preliminary version of the present paper (arXiv: 2101.00142v1 [44]) was posted and now, we have finished analyzing the dewar experiment results. That work is reported in [52]. It includes a combined plot comparing with the limits derived here.

with r the distance between two scatterers. μ is the reduced mass of DM and nuclues, $\mu = m_X m_A/(m_X + m_A)$, and $R_l(r)$ is the radial component of the wave function for partial waves $l = 0, 1, 2\ldots$ The phase shifts δ_l parametrize the asymptotic behavior of the wave function when r goes to infinity

$$\lim_{r\to\infty} R_l(r) \propto \sin(kr - \pi l/2 + \delta_l), \tag{A2}$$

where $k = \mu v$, and v is the relative velocity of the two particles. The differential and total cross section in terms of the phase shifts are given by

$$\frac{d\sigma}{d\Omega} = \frac{1}{k^2}\left|\sum_{l=1}^{\infty}(2l+1)e^{i\delta_l}P_l(\cos\theta)\sin\delta_l\right|^2, \tag{A3}$$

$$\sigma = \frac{4\pi}{k^2}\sum_{l=0}^{\infty}(2l+1)\sin^2(\delta_l). \tag{A4}$$

In the DM detection literature the momentum transfer cross section σ_T is often used,

$$\begin{aligned}\sigma_T &= 2\pi\int\frac{d\sigma}{d\Omega}(1-\cos\theta)d\theta \\ &= \frac{4\pi}{k^2}\sum_{l=0}^{\infty}(l+1)\sin^2(\delta_{l+1}-\delta_l).\end{aligned} \tag{A5}$$

We will see later that in the parameter space we are interested in, s-wave ($l = 0$) scattering is dominant. So there is little difference between (A4) and (A5) and we will use the total cross section (A4) throughout this paper. Now specializing to the Yukawa potential (1) and changing variables to the dimensionless combination

$$\begin{aligned} x &\equiv 2\mu\alpha r, & u_l(x) &\equiv rR_l(r), \\ a &\equiv \frac{v}{2\alpha}, & b &\equiv \frac{2\mu\alpha}{m_\phi}, \end{aligned} \tag{A6}$$

the Schrödinger equation (A1) becomes

$$\left\{\frac{d}{dx^2} + a^2 - \frac{l(l+1)}{x^2} - \tilde{V}(x)\right\}u_l(x) = 0, \tag{A7}$$

where the dimensionless potential is

$$\tilde{V}(x) = -\frac{1}{x}e^{-\frac{x}{b}}. \tag{A8}$$

In this notation the phase shift is given by

$$\lim_{x\to\infty} u_l(x) \propto \sin(ax - \pi l/2 + \delta_l). \tag{A9}$$

The cross sections are

$$\frac{d\sigma}{d\Omega} = \frac{1}{a^2b^2m_\phi^2}\left|\sum_{l=1}^{\infty}(2l+1)e^{i\delta_l}P_l(\cos\theta)\sin\delta_l\right|^2, \tag{A10}$$

$$\sigma = \frac{4\pi}{a^2b^2m_\phi^2}\sum_{l=0}^{\infty}(2l+1)\sin^2(\delta_l), \tag{A11}$$

where $k = abm_\phi$. The phase shift δ_l and σm_ϕ^2 only depend on the dimensionless parameters (a, b). For reference, the (first-order) Born approximation gives

$$\left(\frac{d\sigma}{d\Omega}\right)^{\text{Born}} = \left(\frac{2\mu\alpha}{m_\phi^2 + 4k^2\sin^2\frac{\theta}{2}}\right)^2, \tag{A12}$$

$$\sigma^{\text{Born}} = \frac{16\pi\mu^2\alpha^2}{m_\phi^2(m_\phi^2 + 4k^2)} = \frac{4\pi b^2}{m_\phi^2(1 + 4a^2b^2)}. \tag{A13}$$

Equation (A7) is a second-order differential equation together with the initial condition $u_l(0) = 0, u_l'(0) = 0$ (for regularity of the wave function at $x = 0$). It needs to be solved for $u_l(x)$ with $x \in [0, \infty)$, and δ_l is obtained from $u_l(\infty)$ as in (A9). However, numerically the best we can do is to solve $u_l(x)$ for $x \in [x_i, x_m]$ with sufficiently small(large) but finite $x_i(x_m)$, and match δ_l at $u_l(x_m)$ to achieve appropriate accuracy. The detailed numerical method for the point Yukawa potential is described below. For the extended Yukawa potential, a new scale "c" is introduced and a slight modification is needed:

(1) Since we are changing the initial point from zero to $x_i > 0$, a different initial condition should be used. When x_i is sufficiently small, such that the Yukawa and a^2 terms in Eq. (A7) are subdominant compared to the angular momentum term, the solution is approximately $u_l(x) \propto x^{l+1}$. Ignoring the overall normalization of $u(x)$ since it is irrelevant for determining δ_l, we impose the initial condition,

$$\begin{aligned} u_l(x_i) &= 1, \\ u_l'(x_i) &= \frac{l+1}{x_i}. \end{aligned} \tag{A14}$$

x_i should be small enough for Eq. (A14) to work, and we choose the following condition based on trail and error in our parameter range,

$$\begin{cases} x_i \le \frac{1}{10}\min\left(1, \frac{1}{a}, b\right) & (l = 0) \\ \begin{pmatrix} a^2 \le \frac{1}{10}\frac{l(l+1)}{x_i^2} \\ \frac{1}{x_i}e^{-\frac{x_i}{b}} \le \frac{1}{10}\frac{l(l+1)}{x_i^2} \\ x_i \le \frac{1}{10}x_{it} \end{pmatrix} & (l > 0), \end{cases} \tag{A15}$$

where x_{it} is the smallest classical turning point. (Notice that for $l = 0$ the angular-momentum term disappears and a different condition must be used.) This is our initial guess for a small enough x_i.

(2) We solve Eq. (A7) with the initial condition (A14) for $x \in [x_i, x_m]$. The endpoint x_m is determined so that the Yukawa term is negligible compared to the a^2 term and the angular term. For any potential which is exactly zero for $x \geq x_m$, matching the solution at x_m will give the exact δ_l. The condition for x_m is

$$\begin{cases} \frac{1}{x'_m} e^{-\frac{x'_m}{b}} \leq \frac{1}{10} a^2, \quad x_m \geq x'_m + 5b & (l = 0) \\ \begin{pmatrix} \frac{1}{x_m} e^{-\frac{x_m}{b}} \leq \frac{1}{10} a^2 \\ \frac{1}{x_m} e^{-\frac{x_m}{b}} \leq \frac{1}{10} \frac{l(l+1)}{x_i^2} \\ x_m \geq x_{mt} + 5b \end{pmatrix} & (l > 0), \end{cases} \tag{A16}$$

where x_{mt} is the largest classical turning point. The condition involving x_{mt} is critical since in practice we find the phase shift only starts to converge to its asymptotic value after x_{mt}, where the wave function starts to oscillate like a sine function. The $5b$ is chosen from experience, justified by the fact that b is the only relevant scale introduced by the Yukawa term. This will be our initial guess for a large enough x_m.

(3) At x_m we match $u_l(x)$ to a new asymptotic form, different from Eq. (A9),

$$\lim_{x\to\infty} u_l(x) \propto x e^{i\delta_l} (\cos\delta_l j_l(ax) - \sin\delta_l n_l(ax)) \tag{A17}$$

following [53], where j_l (n_l) is the spherical Bessel (Neumann) function. The corresponding dimensional condition for the original wave function is

$$\lim_{r\to\infty} R_l(r) \propto \cos\delta_l j_l(kr) - \sin\delta_l n_l(kr). \tag{A18}$$

Inverting (A17), the phase shift is given by

$$\delta_l = \arctan\left[\frac{a x_m j'_l(a x_m) - \beta_l j_l(a x_m)}{a x_m n'_l(a x_m) - \beta_l n_l(a x_m)}\right], \quad \text{where } \beta_l \equiv \frac{x_m u'_l(x_m)}{u_l(x_m)} - 1. \tag{A19}$$

(4) Based on the initial guess of (x_i,x_m), we calculate δ_l according to (A19). To check convergence, in other words to test if $x_i(x_m)$ is sufficiently small(large), we first fix x_i and increase x_m in units of b (by the assumption that b is the relevant scale for convergence) until δ_l converges at 1%, to obtain a (x_i,δ_l) pair. Practically, we find δ_l will converge within $x_m + 20b$. Then we decrease x_i by half each time until δ_l converges at 1% with respect to x_i. Our experience shows convergence will be achieved within $2^{-20} x_i$. Finally we obtain δ_l for each (a,b,l).

(5) We calculate σ by summing over l in Eq. (A11). The truncation of the series, $l_{\max}$, is determined by the requirement that $l_{\max}$ contributes to σ less than 1% of the sum of all smaller l, and $\delta_{l_{\max}} < 0.01$. And we check this condition for 10 successive $l_{\max}$ to make sure we arrived at sufficiently large l so that higher l makes ignorable contribution.

2. Phase function method

An alternative way to calculate the phase shift δ_l instead of solving the Schrödinger equation, is the phase function method or variable phase method. See the book by Calogero [54] for details. In our dimensionless parametrization, we define the differential equation obeyed by the phase function $\delta_l(x)$,

$$\delta'_l(x) = a x e^{-\frac{x}{b}} [\cos\delta_l(x) j_l(ax) - \sin\delta_l(x) n_l(ax)]^2 \tag{A20}$$

with the boundary condition

$$\lim_{x\to 0} \delta_l(x) \to \frac{a^{2l+1} x^{2l+2}}{(2l+2)[(2l+1)!!]^2} \to 0$$
$$\lim_{x\to\infty} \delta_l(x) \to \delta_l. \tag{A21}$$

It is clear that the phase function got it is name since its asymptotic value gives the phase shift, $\delta_l(\infty) = \delta_l$. The advantage of the phase-function method is that the phase equation is first-order instead of the second-order Schrödinger equation. The trade-off is that the equation is now nonlinear. In the form described by Eq. (A20), the angular momentum term is eliminated, so we need to integrate to a larger cutoff point x_m to achieve appropriate convergence for δ_l. Overall, the phase function method turns out to be more efficient and has the ability to resolve a much smaller phase shift than the Schrödinger equation method, in certain regions of the parameter space. In obtaining our results for this paper, both methods have been used depending on the parameter regime. Our program is written in Mathematica.

APPENDIX B: APPROXIMATE TREATMENT OF VELOCITY DEPENDENCE OF EXTENDED YUKAWA

If the mediator is heavy ($m_\phi r_0 \gg 1$), so its Compton wavelength is small compared to the size of the nucleus, the extended Yukawa potential can be approximated to a finite square well, where r_0 is identified as the square well width and $V(0)$ is set to be the same for both potentials. This provides us with analytic expression of the cross section, its velocity dependence and the transition velocity v^* near resonance. The scattering length a and effective range r_{eff} can also be easily obtained.

1. Summary of key potentials

(a) *Point Yukawa:* The point Yukawa potential takes the form

$$V(r) = -\frac{\alpha}{r}e^{-\frac{r}{r_\phi}}$$
$$\tilde{V}(x) = -\frac{1}{x}e^{-\frac{x}{b}}, \tag{B1}$$

where we defined

$$b = 2\mu\alpha r_\phi = \frac{2\mu\alpha}{m_\phi}, \tag{B2}$$

$$x = 2\mu\alpha r. \tag{B3}$$

(b) *Extended Yukawa:* The extended Yukawa takes the form

$$V(r) = -\frac{3\alpha}{m_\phi^2 r_0^3}\begin{cases} 1-(1+m_\phi r_0)e^{-m_\phi r_0}\frac{\sinh(m_\phi r)}{m_\phi r} & (r < r_0) \\ [m_\phi r_0 \cosh(m_\phi r_0) - \sinh(m_\phi r_0)]\frac{e^{-m_\phi r}}{m_\phi r} & (r \geq r_0), \end{cases} \tag{B4}$$

$$\tilde{V}(x) = -3\left(\frac{b}{c}\right)^3\begin{cases} \frac{1}{b}-(1+\frac{c}{b})e^{-\frac{c}{b}}\frac{1}{x}\sinh(\frac{x}{b}) & (x < c) \\ [\frac{c}{b}\cosh(\frac{c}{b}) - \sinh(\frac{c}{b})]\frac{1}{x}e^{-\frac{x}{b}} & (x \geq c). \end{cases} \tag{B5}$$

(c) *Finite square well:* The finite square well takes the form

$$V(r) = \begin{cases} -V_0 & (r < r_0) \\ 0 & (r \geq r_0) \end{cases}$$
$$\tilde{V}(x) = \begin{cases} -\tilde{V}_0 & (x < c) \\ 0 & (x \geq c), \end{cases} \tag{B6}$$

where we defined

$$\tilde{V}_0 = \frac{V_0}{2\mu\alpha^2}. \tag{B7}$$

Notice that for a finite square well α and hence c are not *a priori* defined but are introduced in anticipation of making the connection to the extended Yukawa potential.

2. The finite square well as limit of extended Yukawa

Identifying the depth of a finite square well V_0 with $V(0)$ of an extended Yukawa, and keep the radius r_0 as a free parameter of either, we have

$$V_0 = \frac{3\alpha}{m_\phi^2 r_0^3},$$
$$\tilde{V}_0 = \frac{3b^2}{c^3}. \tag{B8}$$

The finite square well can be thought of as a limit of the extended Yukawa when

$$\frac{r_0}{r_\phi} \to \infty, \qquad V_0 = \text{const},$$
$$\frac{c}{b} \to \infty, \qquad \tilde{V}_0 = \text{const}. \tag{B9}$$

Figure 16 compares both potential for different values of c/b.

3. Bound state and scattering state of square well

The condition for the formation a zero-energy bound state is

$$\tilde{V}_0 c^2 = 2\mu r_0^2 V_0 = \left(n + \frac{1}{2}\right)^2 \pi^2, \quad n = 0, 1, 2. \tag{B10}$$

The scattering state phase shift is determined at $r = r_0$ or $x = c$ by

$$\delta_l = \arctan\left[\frac{ac j_l'(ac) - \beta_l j_l(ac)}{ac n_l'(ac) - \beta_l n_l(ac)}\right],$$
$$\beta_l \equiv \frac{Kc j_l'(Kc)}{j_l(Kc)}, \tag{B11}$$

where $j_l'(Kc) \equiv j_l'(z)$ evaluated at $z = Kc$. And $K = \sqrt{a^2 + \tilde{V}_0})$. The following is also true,

$$\delta_l = \arctan\left[\frac{a j_l'(ac) j_l(Kc) - K j_l(ac) j_l'(Kc)}{a n_l'(ac) j_l(Kc) - K n_l(ac) j_l'(Kc)}\right]. \tag{B12}$$

It is also good to remember that Kc and ac are dimensionless and they can be expressed using dimensionfull variables,

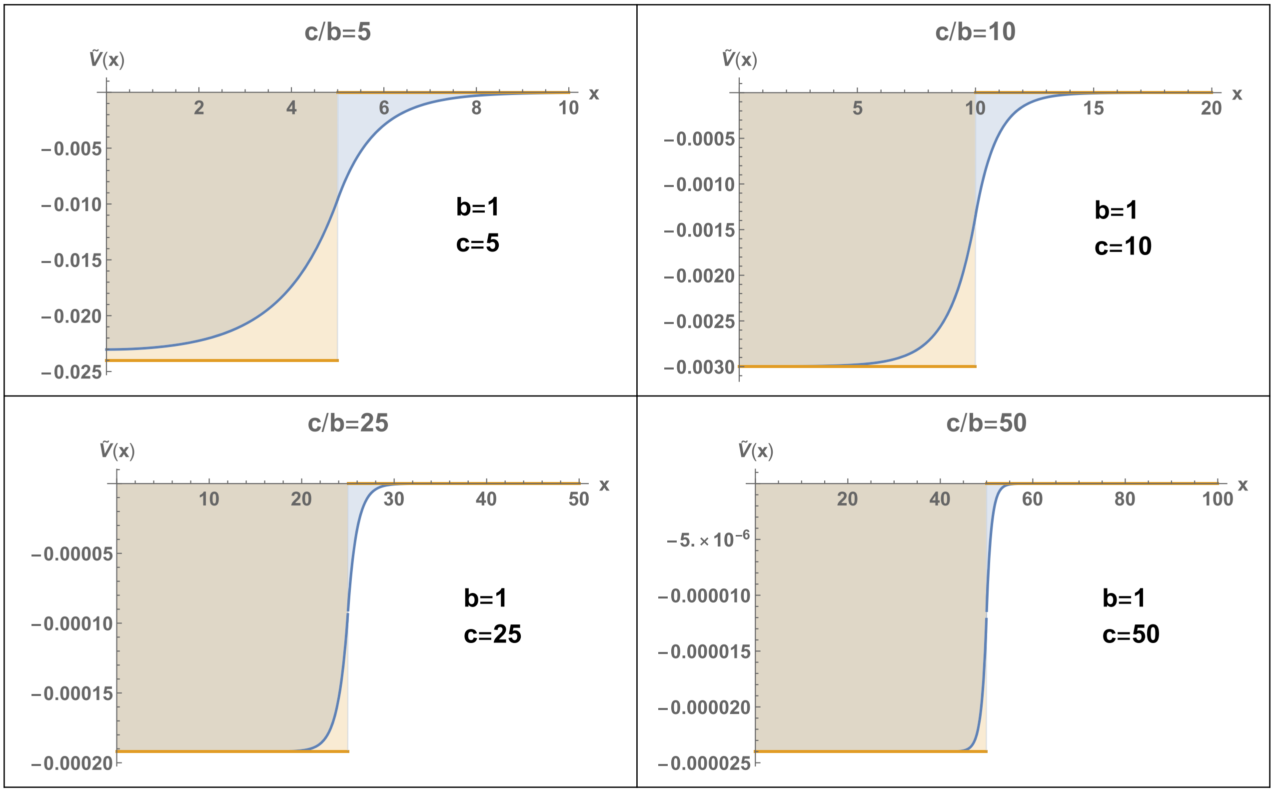

FIG. 16. $\tilde{V}(x)$ for extended Yukawa (blue) versus square well (orange) potential for several parameter values.

$$\begin{aligned} ac &= \frac{v}{2\alpha}\cdot 2\mu\alpha r_0 = \mu v\cdot r_0 = kr_0,\\ Kc &= \sqrt{a^2+\tilde{V}_0}\cdot c = \sqrt{\left(\frac{v}{2\alpha}\right)^2+\frac{V_0}{2\mu\alpha}}\cdot 2\mu\alpha r_0\\ &= \sqrt{(\mu v)^2+2\mu V_0}\cdot r_0\\ &= \sqrt{k^2+2\mu V_0}\cdot r_0 = \kappa r_0, \end{aligned} \tag{B13}$$

where

$$\kappa = \sqrt{k^2+2\mu V_0} = \sqrt{2\mu\left(\frac{k^2}{2\mu}+V_0\right)}. \tag{B14}$$

4. *S*-wave resonance and zero-energy bound state

The s-wave cross section is given by

$$\sigma_0 = \frac{4\pi}{k^2}\sin^2\delta_0 = 4\pi r_0^2\cdot\frac{\sin^2\delta_0}{(kr_0)^2} = 4\pi r_0^2\cdot\frac{\sin^2\delta_0}{(ac)^2} \tag{B15}$$

and the phase shift can be obtained from Eq. (B12)

$$\delta_0 = \arctan\left[\frac{ac\cos(ac)\sin(Kc) - Kc\cos(Kc)\sin(ac)}{ac\sin(ac)\sin(Kc) + Kc\cos(Kc)\cos(ac)}\right]. \tag{B16}$$

The cross section is then

$$\begin{aligned} \frac{\sigma_0}{4\pi r_0^2} &= \frac{1}{(ac)^2}\frac{(Kc\cos(Kc)\sin(ac) - ac\cos(ac)\sin(Kc))^2}{(Kc)^2\cos^2(Kc)+(ac)^2\sin^2(KC)}\\ &= \frac{1}{p^2}\frac{(p\cos p\sin Q - Q\cos Q\sin p)^2}{p^2\sin^2 Q + Q^2\cos^2 Q}, \end{aligned} \tag{B17}$$

where we defined

$$\begin{aligned} p &\equiv ac = kr_0,\\ Q &\equiv Kc = \kappa r_0 = \sqrt{p^2+V^2},\\ V^2 &\equiv \tilde{V}_0 c^2 = 2\mu r_0^2 V_0. \end{aligned} \tag{B18}$$

For low-energy s-wave scattering in the resonant region we have

$$p \ll 1 \le V \sim Q \tag{B19}$$

and a zero-energy bound state appears when $V = (n+1/2)\pi$.

For small p the cross section goes like

$$\frac{\sigma_0}{4\pi r_0^2} \sim \frac{1}{p^2}\frac{p^2(\sin Q - Q\cos Q)^2 + \mathcal{O}(p^4)}{p^2\sin^2 Q + Q^2\cos^2 Q}. \tag{B20}$$

There are three possibilities in the low-energy limit $p \to 0$:

(a) *Constant:* ($Q\cos Q \neq 0$ and $\sin Q - Q\cos Q \neq 0$) In this case the constant term dominates the denominator so that the cross section goes to a constant

$$\frac{\sigma_0}{4\pi r_0^2} \to \frac{1}{p^2}\frac{p^2(\sin Q - Q\cos Q)^2}{Q^2\cos^2 Q} \to \frac{(\sin V - V\cos V)^2}{V^2\cos^2 V}. \tag{B21}$$

(b) *Resonance:* ($Q\cos Q = 0$ and $\sin Q - Q\cos Q \neq 0$) In this case the p^2 term dominates the denominator, and $\cos Q = 0$ so that the cross section goes as p^{-2},

$$\frac{\sigma_0}{4\pi r_0^2} \to \frac{1}{p^2}\frac{p^2(\sin Q - Q\cos Q)^2}{p^2\sin^2 Q} \sim \frac{1}{p^2}. \tag{B22}$$

Because $p \ll 1$, the cross section can be much larger than the geometrical cross section.

(c) *Antiresonance:* ($Q\cos Q \neq 0$ and $\sin Q - Q\cos Q = 0$) In this case the p^2 term in the numerator vanishes, and $\tan Q = Q$. The cross section is suppressed by p^2,

$$\frac{\sigma_0}{4\pi r_0^2} \to \frac{1}{p^2}\frac{\mathcal{O}(p^4)}{Q^2\cos^2 Q} \sim \mathcal{O}(p^2). \tag{B23}$$

So the p-wave contribution starts to be important.

5. Near the resonance

We expand near the resonance to study the velocity dependence behavior of the s-wave cross section. To be precise, we expand Eq. (B17) around $V = (n + 1/2)\pi$,

$$V = \left(n + \frac{1}{2}\right)\pi + \Delta \tag{B24}$$

with $|\Delta| \ll 1$ and $p \ll 1$. We have

$$\begin{aligned}\sigma_0 &= \frac{4\pi r_0^2}{p^2}\frac{(p\cos p\sin Q - Q\cos Q\sin p)^2}{p^2\sin^2 Q + Q^2\cos^2 Q}\\ &= \frac{4\pi r_0^2}{[\Delta_n^2 + \mathcal{O}(\Delta_n^3)] + [1 - \Delta_n + \mathcal{O}(\Delta_n^2)]p^2 + \mathcal{O}(p^3)}\\ &\approx \frac{4\pi}{(\Delta_n/r_0)^2 + (1 - \Delta_n)k^2},\end{aligned} \tag{B25}$$

where we have defined $\Delta_n \equiv (n + 1/2)\pi$ and $|\Delta_n| \ll 1$. Comparing Eq. (B25) with the effective range expansion Eq. (20), we find that for the square well near resonance, the scattering length a and effective range $r_{\rm eff}$ are

$$\begin{aligned}a &= \frac{r_0}{\Delta_n},\\ r_{\rm eff} &= r_0.\end{aligned} \tag{B26}$$

This explicitly shows that near resonance, the scattering length can be much larger than the range of the potential, $|a| \gg r_0$, and how did the effective range $r_{\rm eff}$ get its name. Equation (B25) also tell us the velocity dependence. On resonance where $\Delta_n = 0$, we have the unitarity limit $\sigma_0 = 4\pi/k^2$. Near, but not on resonance, $\Delta_n \neq 0$ and we have

$$\begin{aligned}\sigma_0 &\approx 4\pi\left(\frac{r_0}{\Delta_n}\right)^2, \qquad kr_0 \ll \Delta_n \ll 1,\\ \sigma_0 &\approx \frac{4\pi}{k^2}, \qquad \Delta_n \ll kr_0 \ll 1.\end{aligned} \tag{B27}$$

Recalling the definitions,

$$\begin{aligned}p &= ac = kr_0 = \mu v r_0,\\ \Delta &= V - \frac{2n+1}{2}\pi = \sqrt{\tilde{V}_0}c - \frac{2n+1}{2}\pi\\ &= \sqrt{2\mu V_0}r_0 - \frac{2n+1}{2}\pi\\ &= \sqrt{\frac{3b}{c/b}} - \frac{2n+1}{2}\pi = \sqrt{\frac{6\mu\alpha}{m_\phi^2 r_0}} - \frac{2n+1}{2}\pi,\\ \tilde{V}_0 &= \frac{V_0}{2\mu\alpha^2}(\text{square well}) = \frac{3b^2}{c^3}(\text{Yukawa}),\end{aligned} \tag{B28}$$

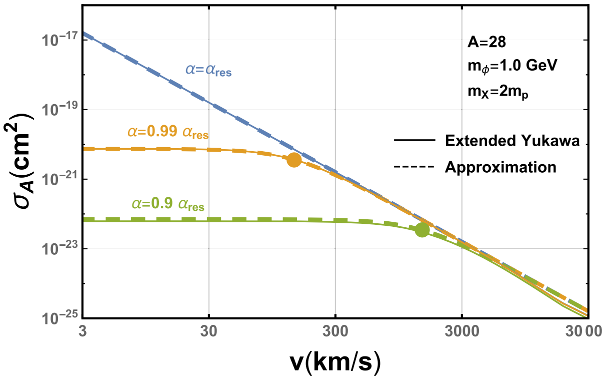

FIG. 17. $\sigma_{28}(v)$ on and near the first resonance. Solid lines are exact numerical results and dashed lines are the approximation from Eq. (B29). The orange and green dots are the transition point $(v^*, \sigma(v^*))$ where v^* is calculated from Eq. (B33) and $\sigma(v^*) = 2\pi/(\mu v^*)^2$. Notice there is a slight difference in the location of the resonance; $\alpha_{\rm res} = 0.129$ for extended Yukawa and $\alpha_{\rm res} = 0.127$ for the approximation (B30). For $A = 28$ and $m_\phi = 1.0$ GeV, we have $c/b = 15.2$.

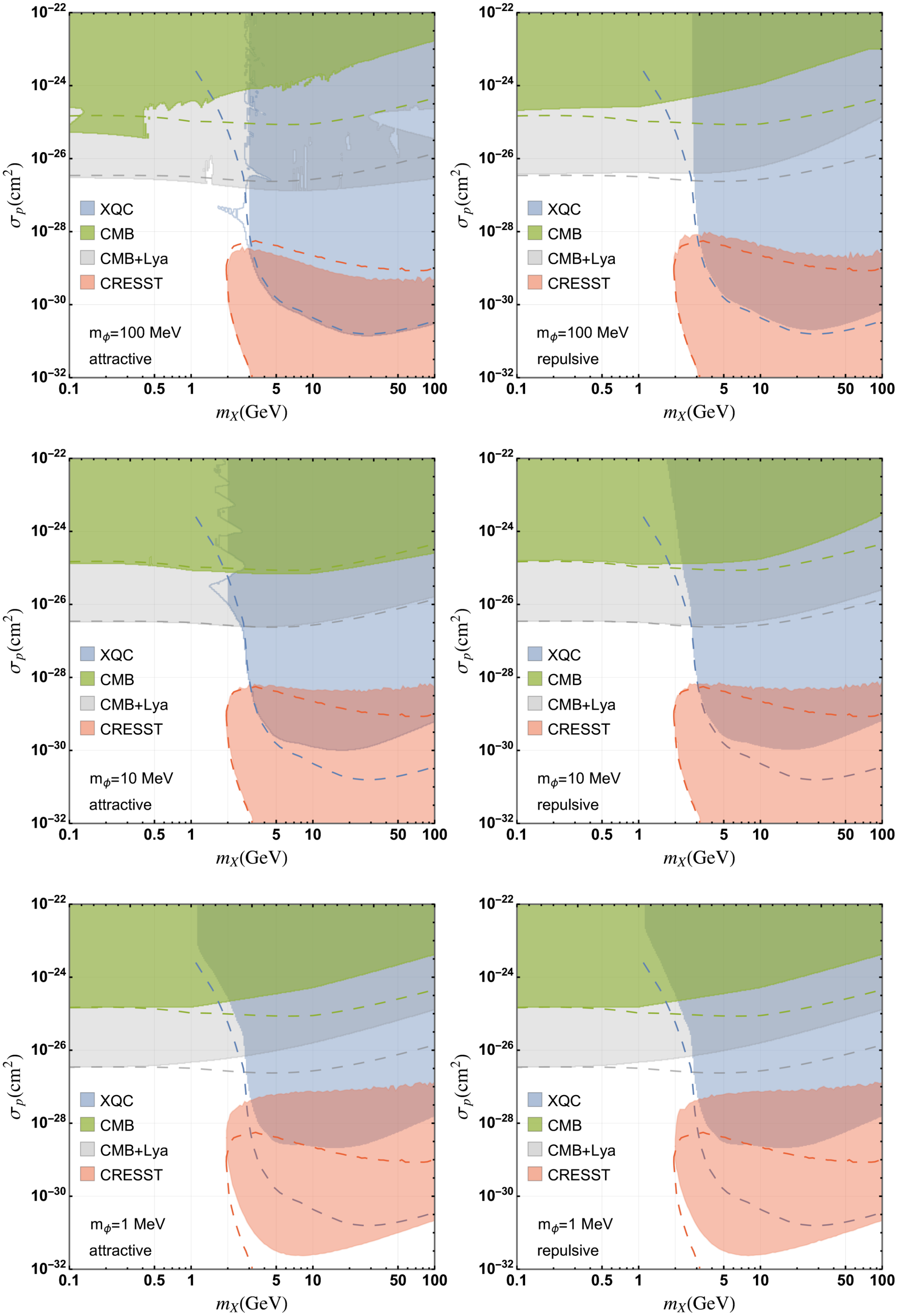

FIG. 18. Exclusion on (σ_p, m_X) for $m_\phi = (1, 10, 100)$ MeV from XQC, CMB (including ^{4}He scattering), and CRESST. The dashed lines indicate the reported limits assuming the Born approximation. The exclusion regions are different from Fig. 14 due to the changed m_ϕ. For example, when $m_\phi = 1$ MeV $\ll 1/r_A$, the cross sections σ_A are all in the Born regime for $\sigma_A \lesssim 10^{-21}$ cm^2, so the cross section does not depend on the sign of the interaction and there is no (anti)resonance. However the commonly used “Born scaling” with A, Eq. (33) still does not work, because it relies on the applicability of the low-energy condition, $\mu v \ll m_\phi$, which is violated with such small m_ϕ.

and reexpressing Eq. (B25) in physical variables for the case of the first resonance, we have

$$\sigma \approx \frac{4\pi}{\mu^2 v^2 + \frac{3\mu\pi^2}{2m_\phi^2 r_0^3}(\sqrt{\alpha} - \sqrt{\alpha_{\rm res}})^2}, \tag{B29}$$

where

$$\alpha_{\rm res} = \left(\frac{\pi}{2}\right)^2 \frac{m_\phi^2 r_0}{6\mu}. \tag{B30}$$

Thus,

$$\sigma \to 4\pi/(\mu v)^2 \quad v \gg v^*, \tag{B31}$$

and

$$\sigma \to \frac{8m_\phi^2 r_0^3}{3\pi\mu(\sqrt{\alpha} - \sqrt{\alpha_{\rm res}})^2} \quad v \ll v^*, \tag{B32}$$

with

$$v^* \equiv \frac{\pi|\sqrt{\alpha} - \sqrt{\alpha_{\rm res}}|}{m_\phi r_0\sqrt{2\mu r_0/3}}. \tag{B33}$$

Figure 17 shows how well the approximations Eqs. (B31)–(B33) approximate the exact velocity dependence for A = 28 (Si) near the first resonance.

APPENDIX C: LIMITS FOR SMALL m_ϕ

Figure 18 shows the constraints from smaller mediator mass, $m_\phi = (1, 10, 100)$ MeV.

[1] J. Fan, M. Reece, and L.-T. Wang, J. Cosmol. Astropart. Phys. 11 (2010) 042.

[2] G. Jungman, M. Kamionkowski, and K. Griest, Phys. Rep. **267**, 195 (1996).

[3] M. Lisanti, in Chapter 7: Lectures on dark matter physics, in *New Frontiers in Fields and Strings* (World Scientific, Singapore, 2017), pp. 399–446.

[4] G. R. Farrar, arXiv:1708.08951.

[5] G. R. Farrar, arXiv:1805.03723.

[6] G. R. Farrar, Z. Wang, and X. Xu, arXiv:2007.10378.

[7] C. Dvorkin, K. Blum, and M. Kamionkowski, Phys. Rev. D **89**, 023519 (2014).

[8] V. Gluscevic and K. K. Boddy, Phys. Rev. Lett. **121**, 081301 (2018).

[9] W. L. Xu, C. Dvorkin, and A. Chael, Phys. Rev. D **97**, 103530 (2018).

[10] A. L. Erickcek, P. J. Steinhardt, D. McCammon, and P. C. McGuire, Phys. Rev. D **76**, 042007 (2007).

[11] M. S. Mahdawi and G. R. Farrar, J. Cosmol. Astropart. Phys. 12 (2017) 004.

[12] M. S. Mahdawi and G. R. Farrar, J. Cosmol. Astropart. Phys. 10 (2018) 007.

[13] G. D. Starkman, A. Gould, R. Esmailzadeh, and S. Dimopoulos, Phys. Rev. D **41**, 3594 (1990).

[14] X. Xu and G. Farrar, in *APS April Meeting Abstracts*, APS Meeting Abstracts Vol. 2019 (American Physics Society, 2019), p. Z10.002.

[15] M. C. Digman, C. V. Cappiello, J. F. Beacom, C. M. Hirata, and A. H. G. Peter, Phys. Rev. D **100**, 063013 (2019).

[16] G. Angloher *et al.* (CRESST Collaboration), Eur. Phys. J. C **77**, 637 (2017).

[17] Y. Bai and P. J. Fox, J. High Energy Phys. 11 (2009) 052.

[18] A. Sommerfeld, Ann. Phys. (Berlin) **403**, 257 (1931).

[19] N. Arkani-Hamed, D. P. Finkbeiner, T. R. Slatyer, and N. Weiner, Phys. Rev. D **79**, 015014 (2009).

[20] P. Agrawal, A. Parikh, and M. Reece, J. High Energy Phys. 10 (2020) 191.

[21] G. R. Farrar and G. Zaharijas, Phys. Lett. B **559**, 223 (2003); **575**, 358(E) (2003).

[22] M. R. Buckley and P. J. Fox, Phys. Rev. D **81**, 083522 (2010).

[23] S. A. Khrapak, A. V. Ivlev, G. E. Morfill, and S. K. Zhdanov, Phys. Rev. Lett. **90**, 225002 (2003).

[24] A. Loeb and N. Weiner, Phys. Rev. Lett. **106**, 171302 (2011).

[25] J. J. Sakurai and J. Napolitano, *Modern Quantum Mechanics* (Addison-Wesley, Reading, MA, 2011), 2nd ed.

[26] H. A. Bethe, Phys. Rev. **76**, 38 (1949).

[27] C. L. Blackley, P. S. Julienne, and J. M. Hutson, Phys. Rev. A **89**, 042701 (2014).

[28] S. K. Adhikari, Eur. J. Phys. **39**, 055403 (2018).

[29] R. W. McAllister and R. Hofstadter, Phys. Rev. **102**, 851 (1956).

[30] D. R. Yennie, D. G. Ravenhall, and R. N. Wilson, Phys. Rev. **95**, 500 (1954).

[31] X. Roca-Maza, M. Centelles, F. Salvat, and X. Viñas, Phys. Rev. C **78**, 044332 (2008).

[32] R. Hofstadter, Rev. Mod. Phys. **28**, 214 (1956).

[33] J. Lewin and P. Smith, Astropart. Phys. **6**, 87 (1996).

[34] R. H. Helm, Phys. Rev. **104**, 1466 (1956).

[35] D. McCammon, R. Almy, E. Apodaca, W. B. Tiest, W. Cui, S. Deiker, M. Galeazzi, M. Juda, A. Lesser, T. Mihara *et al.*, Astrophys. J. **576**, 188 (2002).

[36] B. D. Wandelt, R. Dave, G. R. Farrar, P. C. McGuire, D. N. Spergel, and P. J. Steinhardt, in *4th International Symposium on Sources and Detection of Dark Matter in the Universe (DM 2000)* (Springer Berlin, Heidelberg, 2000), pp. 263–274, arXiv:astro-ph/0006344.

[37] G. Zaharijas and G. R. Farrar, Phys. Rev. D **72**, 083502 (2005).

[38] L. Hui, J. P. Ostriker, S. Tremaine, and E. Witten, Phys. Rev. D **95**, 043541 (2017).
[39] N. Mandelker, F. C. van den Bosch, V. Springel, and F. van de Voort, Astrophys. J. **881**, L20 (2019).
[40] E. O. Nadler *et al.* (DES Collaboration), Phys. Rev. Lett. **126**, 091101 (2021).
[41] R. Strauss *et al.*, Eur. Phys. J. C **77**, 506 (2017).
[42] R. Strauss, J. Rothe, G. Angloher, A. Bento, A. Gütlein, D. Hauff, H. Kluck, M. Mancuso, L. Oberauer, F. Petricca, F. Pröbst, J. Schieck, S. Schönert, W. Seidel, and L. Stodolsky, Phys. Rev. D **96**, 022009 (2017).
[43] D. Wadekar and G. R. Farrar, Phys. Rev. D **103**, 123028 (2021).
[44] X. Xu and G. R. Farrar, arXiv:2101.00142v1.
[45] K. K. Rogers, C. Dvorkin, and H. V. Peiris, Phys. Rev. Lett. **128**, 171301 (2022).
[46] E. O. Nadler, V. Gluscevic, K. K. Boddy, and R. H. Wechsler, Astrophys. J. Lett. **878**, L32 (2019); **897**, L46(E) (2020);
[47] C. V. Cappiello, J. I. Collar, and J. F. Beacom, Phys. Rev. D **103**, 023019 (2021).
[48] S. A. Khrapak, A. V. Ivlev, G. E. Morfill, S. K. Zhdanov, and H. M. Thomas, IEEE Trans. Plasma Sci. **32**, 555 (2004).
[49] M. Digman (private communication).
[50] D. A. Neufeld and D. J. Brach-Neufeld, Astrophys. J. **877**, 8 (2019).
[51] D. A. Neufeld, G. R. Farrar, and C. F. McKee, Astrophys. J. **866**, 111 (2018).
[52] X. Xu and G. R. Farrar, arXiv:2112.00707.
[53] S. Tulin, H.-B. Yu, and K. M. Zurek, Phys. Rev. D **87**, 115007 (2013).
[54] F. Calogero, *Variable Phase Approach to Potential Scattering* (Elsevier, New York, 1967), 1st ed.